UNIVERSIDAD SAN FRANCISCO DE QUITO USFQ Colegio de Posgrados

Chiral Molecular Circuits and Spin Detection

David Llerena Aveiga

Ernesto Medina, PhD Director de Trabajo de Titulación

Trabajo de titulación presentado como requisito para la obtención del titulo de Magíster en Física

Quito, December 21, 2024

Dario Niebieskikwiat

Doctor en Física

UNIVERSIDAD SAN FRANCISCO DE QUITO USFQ Colegio de Posgrados

HOJA DE APROBACIÓN DE TRABAJO DE TITULACIÓN

Chiral Molecular Circuits and Spin Detection

David Llerena Aveiga

Nombre del Director del Programa:

Título académico:

Director del programa de:

Nombre del Decano del Colegio Académico:

Título académico:

Doctor en Física

Maestría en Física

Eduardo Alba

Título académico:

Doctor en Ciencias Matemáticas

Decano del Colegio:

Colegio de Ciencias e Ingeniería

Nombre del Decano del Colegio de Posgrados:

Título académico:

2

© Derechos de Autor

Por medio del presente documento certifico que he leído todas las Políticas y Manuales

de la Universidad San Francisco de Quito USFQ, incluyendo la Política de Propiedad Int-

electual USFQ, y estoy de acuerdo con su contenido, por lo que los derechos de propiedad

intelectual del presente trabajo quedan sujetos a lo dispuesto en esas Políticas.

Asimismo, autorizo a la USFQ para que realice la digitalización y publicación de este

trabajo en el repositorio virtual, de conformidad a lo dispuesto en la Ley Orgánica de

Educación Superior del Ecuador.

Nombres y apellidos:

David Llerena Aveiga

Código:

00335017

Cédula de Identidad:

1750995738

Lugar y fecha:

Quito, December 21, 2024

ACLARACIÓN PARA LA PUBLICACIÓN

Nota: El presente trabajo, en su totalidad o cualquiera de sus partes, no debe ser considerado como una publicación, incluso a pesar de estar disponible sin restricciones a través de un repositorio institucional. Esta declaración se alinea con las prácticas y recomendaciones presentadas por el Committee on Publication Ethics COPE descritas por Barbour et al. (2017) Discussion document on best practice for issues around theses publishing, disponible en http://bit.ly/COPETheses

UNPUBLISHED DOCUMENT

Note: The following capstone project is available through Universidad San Francisco de Quito USFQ institutional repository. Nonetheless, this project – in whole or in part – should not be considered a publication. This statement follows the recommendations presented by the Committee on Publication Ethics COPE described by Barbour et al. (2017) Discussion document on best practice for issues around theses publishing available on http://bit.ly/COPETheses

Agradecimientos

Quiero agradecer enormemente a Ernesto Medina, supervisor de este trabajo, por su guía, confianza y apoyo a largo de este trabajo. Sin duda su concimiento y dedicación me impulsaron durante este preoceso y me han permitido crecer como investigador. Agradezco también a Pedro Ducos, co-supervisor, quien fue de gran apoyo en el desarrollo experimental aquí presentado.

Agradezco profundamente a Chrisitian Luciani, quien siempre estuvo dispuesto a facilitarme en lo más posibile este proceso experimental. A Werner Brämer, por su invaluable ayuda en la primera parte del proyecto y sus consejos que permitieron que llegara hasta acá. Un fuerte agradecimiento a Dennis Cazar, Malena Loza y Krutskaya Yépez por su colaboración y ayuda.

Con todo el corazón agradezco a mi familia, Nancy, Mauricio, Alex y Flun. Han estado a mi lado durante todo este proceso y siempre me han apoyado en cada paso del camino. A Valeria, con quien pasamos grandes retos juntos y compartimos todo este camino; su apoyo y amistad los llevo siempre en mi corazón. A Noe por su constante amor y confianza que en muchas ocasiones necesité y a veces no era capaz de encontrar en mí.

Agradezco a la USFQ por la oportunidad de pertenecer a este programa de posgrado de alta calidad.

Resumen

El problema de la selectividad de espín inducida por la quiralidad molecular ha sucitado un gran interés, ya que sugiere funciones para la polarización de espín en procesos biológicos y promete aplicaciones espintrónicas que aprovechan el débil acoplamiento espín-órbita de las moléculas orgánicas como única fuente de actividad de espín. Desde el punto de vista teórico, el enfoque se ha basado en modelos microscópicos cuánticos que calculan la conductancia a partir de la fórmula de Landauer-Buttiker. Este enfoque omite características físicas experimentales importantes, como la reciprocidad, ya que no incorpora el mecanismo de medición de espín limitado por las relaciones de reciprocidad. Desde el punto de vista experimental, la mayoría de los enfoques que evidencian los efectos del filtrado de espín son circuitos complejos de una sola molécula a partir de monocapas autoensambladas de moléculas quirales sobre tricapas de metal-óxido-ferro relativamente grandes. En este trabajo, abordamos el problema teórico desde el formalismo de la matriz de transporte que incluye explícitamente el dispositivo de medición de espín y reproduce los teoremas de reciprocidad. Este formalismo propone dos formas de medir la polarización de espín en el régimen lineal: a través de una medición de tres puntas o introduciendo una ruptura de la simetría de reversión temporal en el modelo de la molécula quiral. En el aspecto experimental, abordamos el filtrado de espín molecular mediante el desarrollo de un dispositivo break junction, sentando los primeros pasos en la medición de la actividad de espín en uniones moleculares quirales.

Palabras clave: Selección de espín, quiralidad molecular, polarización de espín, reciprocidad, formalismo de la matrix de transporte, break junction, juntas moleculares.

Abstract

The problem of spin selectivity induced by molecular chirality has garnered high interest since it suggests roles for spin polarization in biological processes and promises spintronic applications harnessing the weak spin-orbit coupling of organic molecules as the sole source of spin activity. On the theoretical side, the approach has been from quantum microscopic models computing the conductance from the Landauer-Buttiker formula. This approach misses important experimental physical features such as reciprocity since it does not incorporate the spin measuring mechanism limited by reciprocity relations. On the experimental side, most approaches that evidence spin filtering effects are complex single-molecule circuits from self-assembled monolayers of chiral molecules on relatively large metal-oxide-ferro trilayers. We address the theoretical problem from the transport matrix formalism that explicitly includes the spin measurement device and reproduces the reciprocity theorems. This formalism proposes two ways to measure spin polarization in the linear regime: through a three-point measurement or by introducing time-reversal symmetry breaking in the chiral molecule model. On the experimental side, we approach molecular spin filtering by implementing the break junction device, implementing the first steps in measuring spin activity in chiral molecular junctions.

Keywords: Spin selectivity, molecular chirality, spin polarization, reciprocity, transport matrix formalism, break junction, molecular junctions.

Contents

1	Intr	oducti	on	12			
2	The	Theoretical Background					
	2.1	Standa	ard Model of Spin Injection	16			
		2.1.1	Spin Injection $F \Rightarrow N$	17			
		2.1.2	Silsbee-Johnson Spin-Charge Coupling	21			
	2.2	Electro	on Transport in atomic-sized Contacts	26			
	2.3	Transp	port Matrix Formalism	28			
		2.3.1	Spin-Charge Transport in the Chiral Component	29			
		2.3.2	Spin-Charge Transport in the achiral Ferromagnetic Tunnel Junction (FMTJ)	32			
		2.3.3	Spin-Charge Transport in 2T geometry	33			
	2.4	_	Binding Example Model of the Electronic Transport Through a Chi- olecule	35			
3	Tow	ard Ti	cansport in Nanoscale structures: Experimental Set-up	40			
	3.1	Mecha	nically Controlled Break Junction	40			
	3.2	Electro	onics	41			
	3.3	Homo	metallic Junctions	44			
	3.4	Bimet	allic Samples	45			

4	Results			
	4.1	Spin-Charge Transport in 3T Geometry	47	
		4.1.1 Application of the Transport Matrix Model	49	
	4.2	Homometallic Junction	56	
	4.3	Preliminary Bimetallic Junction Results	58	
5	Con	clusions	61	
	5.1	Future Work	63	
Re	References			
\mathbf{A}	Trai	nsport Matrix for the Chiral Component	70	
В	Trai	nsport Matrix for the FMTJ	74	
\mathbf{C}	2T :	Spin-Charge Transport	76	

List of Figures

1.1	CISS detection set-up on PSI	13
2.1	Scheme of a F/N junction	17
2.2	Spatial profile of the spin accumulation μ_s across the junction	24
2.3	Illustration of Landauer's representation of an electronic transport experiment	27
2.4	Generic 2T circuit containing a chiral component connected in series with a ferromagnet with a node in the middle	28
2.5	Representation of the spin-dependent transmission and reflection for (a) ideal CISS effect and (b) ferromagnetic conductor	29
2.6	Structure of the example model for the molecule	36
3.1	Diagram and picture of the MCBJ device	41
3.2	Circuit diagram of the electronics connected to the MCBJ	42
3.3	Aluminum enclosure of the electronics of the MCBJ device	43
3.4	Notching mechanism for the preparation of homometallic junction samples.	44
3.5	Sample placed on the PLA flexible substrate. A diagram can be seen in the upper part, while a picture of the real montage can be seen in the lower part	45
3.6	Three-point bending device for the bimetallic junction sample preparations. Bimetallic Sample of Au-Ni	46
4.1	Proposed 3T circuit geometry	48

4.2	Spin valve 2T geometry circuit with two ferromagnets FL and FR in series.	50
4.3	Example I-V curves due to the introduction of time-reversal symmetry breaking in the molecule's transport matrix	56
4.4	Results of the measurements taken on the Au-Au junction	57
4.5	Configurations obtained from MD simulations right before first contact or just after breaking	57
4.6	Rupture conductance histograms of homometallic and bimetallic atomic-sized junctions	59

Chapter 1

Introduction

Chiral molecules, ubiquitous in biological systems, such as amino acids, oligopeptides, proteins, and many alpha-helical structures, are involved in many electron transfer processes [1, 2]. The chirality of molecules has been linked to electron spin polarization since the theoretical work of Farago [3, 4], who found that point chiral molecules coupled to spin through the spin-orbit coupling (SOC) and generated an angular-dependent polarization. Later, Kessler's experiments for point chiral molecules in the gas phase yielded a very small but measurable polarization of $10^{-4}\%$ with enhanced SOC bonded ad-hoc with heavy atoms [5]. Theoretical developments Blum and Thompson [6, 7] used scattering theory in the Born approximation to account for the spin active effects of gas phase chiral molecules.

Due to the small spin polarizing effects, interest was lost for a while until the ground-breaking experimental work of Naaman's group [8], where they worked on self-assembled monolayers (SAM) of small aminoacids. Using a Mott detector, they evidenced strong spin-polarizing effects for photo-emitted electrons through the SAM. The same set-up was later used with double-stranded DNA [9] yielded polarizations exceeding 60% measured directly of the transmitted photoelectrons from the Au substrate through the SAM at room temperature. The strong contrast with Kessler's results led to the belief that this

could be a cooperative effect. Still, but later single molecule measurements on double-stranded DNA using a conductive-prove atomic force microscope (c-AFM) [10], led to even stronger polarizations of 60 - 70% from single molecule effects, surpassing that of any known system at room temperature. As a reference, spin polarization achieved by different densities of state of opposite spin electrons in a ferromagnet leads only to polarizations of the order of 20%. This led to coining the term *Chirally Induced Spin Selectivity* (CISS), where the minimal ingredients were thought to be chirality and the SOC associated with chiral centers.

Following these studies, many works have determined CISS effects on different organic chiral molecules such as peptides [11, 12] and DNA [9, 10]. It has also been studied in inorganic chiral materials [13]. In the work by Naaman and Carmeli [14], they confirmed high spin selectivity by measuring spin polarization on transmitted electrons through a photosystem I SAM using a spintronic device and its temperature dependence. They found that spin selectivity peaked at 300 K and vanished at temperatures below 150 K by measuring the emf developed between the nickel and silver layers of a tunnel junction, separated by a slim insulating AlOx layer as is depicted in Fig. 1.1.

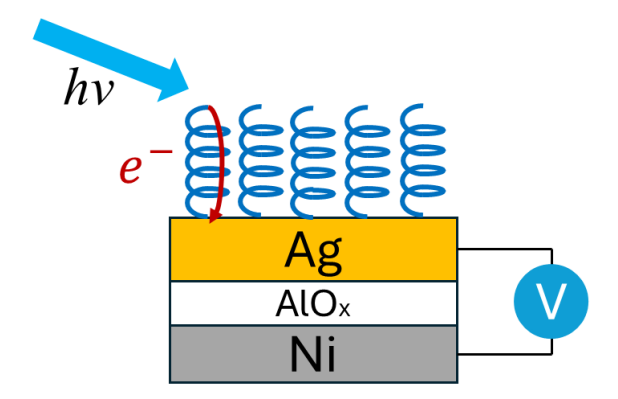


Figure 1.1: PSI monolayers absorbed onto the silver surface. Electron transfer begins after photoexcitation on the primary donor P700. The potential difference between the Ni and the Ag depends on the spin selection by the PSI and the Ni magnetization direction. Adapted from ref. [14].

Single-molecule CISS measurements have also been carried out using a scanning tunneling microscopy break junction (STM-BJ) set-up on peptides [11], leading to conductance polarization of 60% and 57% for the left and right isomer respectively. Other recent

works have shown CISS manifestation at the single molecule level through single helical hydrocarbon molecules showing magnetochiral asymmetries up to 50% in the conductance using a spin-polarized STM [15], and in newly developed oligo(phenylene)ethynylene molecular junctions using STM-BJ method [16].

Several theoretical approaches have been made to explain the CISS effects observed in the experiments. Models using a tight-binding (TB) approximation considering a helical structure of partially filled orbitals attached to the bases [17], evidencing the SO magnitude in the transport problem to be in the order of meV given that the chirality is nonzero. Other models discretize a continuum model where the SO is obtained from the Pauli equation (non-relativistic limit of Dirac equation) in both helical structures and an achiral nanotube [18, 19, 20].

Experimental determinations of CISS have been mostly based on two-terminal (2T) geometry set-ups. Most models are time-reversal invariant due to the SO coupling breaking space inversion symmetry but preserving time-reversal. Because of this, reciprocity theorems dictate that in 2T set-ups, no spin polarization can occur in the linear-response regime [21, 22]. The reciprocity theorem requires that G(H, M) = G(-H, -M); hence, the ferromagnetic detector with a magnetization M can not distinguish any spin polarization no matter the chiral structure and the SO coupling magnitude [23]. To elude this dilemma and remain in linear response, time-reversal symmetry in the chiral molecule must be broken. This can be done by effectively adding a third probe to the molecule. This probe gives rise to non-unitary effects, such as dephasing, that break the time-reversal symmetry. Hence, reciprocity theorems no longer apply, and spin polarization ensues. This third probe was effectively included in the model of Guo and Sun [18], where they demonstrated that no spin polarization is possible without the decoherence probe, even if the helical structure is present and SO coupling is strong.

In this manuscript, we tackle the theoretical problem from the transport matrix formalism developed by Yang Xu and Van Wees [22]. We propose two possible ways of detecting spin polarization in two-terminal set-ups, avoiding the reciprocity problem in the linear regime: by connecting a third probe to the circuit's node and by introducing a small time-reversal asymmetry perturbation in the chiral molecule transport matrix. We also validate this model by looking at the classical spin valve configuration with two ferromagnets and arriving at the GMR and TMR results. On the experimental level, we develop a break junction device that will allow single-molecule measurements. We use the device to study electron transport through homometallic Au-Au and bimetallic Au-Ni junctions by measuring conductance during contact rupture and building conductance histograms at ambient conditions, laying the foundations to study CISS through oligopeptides in the built device.

Chapter 2

Theoretical Background

2.1 Standard Model of Spin Injection

The transfer of spin-polarized electrons from a ferromagnetic (F) conductor to a nonmagnetic (N) conductor forms the foundation of spintronic devices, with the process being referred to as spin injection. This section presents the calculations that lead to the formation of a spin accumulation at the interface of an F/N junction under two study cases: spin injection from F to N without any external spin pumping and spin extraction from N to F, where an external circuit maintains a non-equilibrium spin accumulation at the far end of the nonmagnetic conductor (note that this is our case of interest). For these study cases' complete description and step-by-step derivation, refer to Fabian et al., [24] semiconductors spintronics review.

Throughout this treatment, it is considered that both bulk conductors F and N have dimensions larger than their corresponding spin diffusion lengths ($L_F \ll L_{sF}$ and $L_N \ll L_{sN}$). This length represents the distance at which spin accumulation at each region has been reduced to 1/e percent.

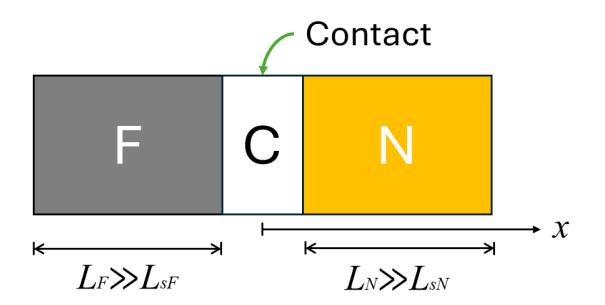


Figure 2.1: Scheme of a F/N junction. The ferromagnet (F) has a width L_F , and the nonmagnetic conductor (N) has a width L_N . Both conductors are assumed to have their physical widths larger than their spin diffusion lengths L_{sF} and L_{sN} , respectively. The contact region of the junction is C, assumed to be infinitely narrow, thus there is a discontinuity at x = 0. Adapted from ref. [24].

2.1.1 Spin Injection $F \Rightarrow N$

We consider that spin is injected from the ferromagnet onto the nonmagnetic conductor. It is assumed that $\mu_{sF}(-\infty) = \mu_{sN}(+\infty) = 0$, that is, spin accumulation only exists at the interface.

The following definitions are required for all the calculations:

$$g = g_{\uparrow} + g_{\downarrow}, \quad gs_{=}g_{\uparrow} - g_{\downarrow}, \tag{2.1}$$

$$\sigma = \sigma_{\uparrow} + \sigma_{\downarrow}, \quad \sigma_s = \sigma_{\uparrow} - \sigma_{\downarrow},$$
 (2.2)

$$\mu = (\mu_{\uparrow} + \mu_{\perp})/2, \quad \mu_s = (\mu_{\uparrow} - \mu_{\perp})/2,$$
 (2.3)

where $g_{\uparrow(\downarrow)}$ is the spin-specific density of states per unit volume, g is the total density of states; $\sigma_{\uparrow(\downarrow)}$ is the spin-specific conductivity, and σ is the total conductivity; $\mu_{\uparrow(\downarrow)}$ is the spin-specific electrochemical potential, μ is the total electrochemical potential, and μ_s is denominated as spin accumulation.

The spin diffusion equation (2.4) can be solved in both regions of the spin detector (F and N, C is not considered a region),

$$\nabla^2 \mu_s = \frac{\mu_s}{L_s^2},\tag{2.4}$$

where L_s is the generalized spin diffusion length given by,

$$L_s = \sqrt{\overline{D}\tau_s}x. {2.5}$$

 $\overline{\mathbf{D}}$ is diffusivity defined as,

$$\overline{D} = \frac{g}{\frac{g_{\uparrow}}{D_{\downarrow}} + \frac{g_{\downarrow}}{D_{\uparrow}}} = \frac{1}{e^2} \frac{g}{g_{\uparrow} g_{\downarrow}} \frac{\sigma_{\uparrow} \sigma_{\downarrow}}{\sigma}, \tag{2.6}$$

For a degenerate conductor (metal), the current spin polarization $P_j = j_s/j$ is given by,

$$P_j = P_\sigma + \frac{1}{j} 4\nabla \mu_s \frac{\sigma_\uparrow \sigma_\downarrow}{\sigma},\tag{2.7}$$

where $P_{\sigma} = \sigma_s/\sigma$ is the spin polarization of the conductivity. The electric (charge) current density j is defined as

$$j = -eJ = \sigma E + eD\frac{\partial n}{\partial x},\tag{2.8}$$

where J is the electron (particle) current density, E is the electric field magnitude, D is the diffusivity, and n is the density of electrons. The first goal is to find $P_j(x=0)$ that determines the spin accumulation $\mu_{sN}(0)$. Thus, the spin diffusion equation for the F and N regions considering the boundary conditions $\mu_{sF}(-\infty) = \mu_{sN}(+\infty) = 0$ yields,

$$\mu_{sF}(x) = \mu_{sF}(0)e^{x/L_{sF}},$$

$$\Rightarrow \nabla \mu_{sF} = \frac{\mu_{sF}}{L_{sF}},$$
(2.9)

$$\mu_{sN}(x) = \mu_{sN}(0)e^{-x/L_{sN}},$$

$$\Rightarrow \nabla \mu_{sN} = -\frac{\mu_{sN}}{L_{sN}},$$
(2.10)

respectively. In the nonmagnetic conductor N, $P_{\sigma N} = 0$, since $\sigma_{N\uparrow} = \sigma_{N\downarrow} = \sigma_N/2$ (no spin preference in the conductivity).

Thus, rewriting (2.7) for each region,

$$P_{jF}(0) = P_{\sigma F} + \frac{1}{j} \frac{\mu_{sF(0)}}{R_F}, \tag{2.11}$$

$$\Rightarrow j_{sF}(0) = jP_{\sigma F} + \frac{\mu_{sF(0)}}{R_F}, \tag{2.12}$$

$$P_{jN}(0) = -\frac{1}{j} \frac{\mu_{sN}(0)}{R_N}, \tag{2.13}$$

$$\Rightarrow j_{sN}(0) = -\frac{\mu_{sN(0)}}{R_N},\tag{2.14}$$

where R_F and R_N are the effective resistances for each conductor that appear in the spin-polarized transport,

$$R_F = \frac{\sigma_F}{4\sigma_{F\uparrow}\sigma_{F\downarrow}} L_{sF},\tag{2.15}$$

$$R_N = \frac{L_{sN}}{\sigma_N}. (2.16)$$

From (2.13), if $P_{jN}(0)$ is known, then the spin accumulation $\mu_{sN}(0)$ can be calculated

$$\mu_{sN}(0) = -jP_{jN}(0)R_N = -j_{sN}(0)R_N. \tag{2.17}$$

Note that because of R_N , the spin accumulation at N grows with L_{sN} .

Now, we analyze the contact region at x = 0. Since it is located at a single point, the electrochemical potential is discontinuous; thus, it is impossible to define gradients. Instead, the currents are defined by

$$j_{\uparrow} = G_{\uparrow}[\mu_{\uparrow N}(0) - \mu_{\uparrow F}(0)] = G_{\uparrow} \Delta \mu_{\uparrow}(0), \qquad (2.18)$$

$$j_{\downarrow} = G_{\downarrow}[\mu_{\downarrow N}(0) - \mu_{\downarrow F}(0)] = G_{\downarrow} \Delta \mu_{\downarrow}(0), \qquad (2.19)$$

where $G_{\uparrow(\downarrow)}$ is the spin-dependent conductance of the contact instead of conductivity σ as in the bulks of both regions. Spin and charge currents are

$$j = G\Delta\mu(0) + G_s\Delta\mu_s(0), \tag{2.20}$$

$$j_s = G_s \Delta \mu(0) + G \Delta \mu_s(0). \tag{2.21}$$

Eliminating $\Delta\mu$ from (2.20) and substituting into (2.21) yields

$$j_s = P_G j + \frac{\Delta \mu_s(0)}{R_C},\tag{2.22}$$

$$R_C = \frac{G}{4G_{\uparrow}G_{\downarrow}},\tag{2.23}$$

where R_C is the effective resistance of the contact region and $P_G = (G_{\uparrow} - G_{\downarrow})/G$ is conductance spin polarization. The current spin polarization at the contact is obtained from (2.22),

$$P_{jc} = P_G + \frac{1}{j} \frac{\Delta \mu_s(0)}{R_C}.$$
 (2.24)

Now, there are three equations for $P_j(0)$ at both regions and at the interface: (2.11), (2.13), and (2.24); and five unknowns: $P_{jF}(0)$, $P_{jN}(0)$, $P_{jC}(0)$, $\mu_{sF}(0)$, and $\mu_{sN}(0)$. To solve this, an approximation is used: at the contact, the spin current must be continuous; thus,

$$P_{jF}(0) = P_{jN}(0) = P_{jC} \equiv P_j. \tag{2.25}$$

This assumption is justified if spin-flip scattering can be neglected at the contact (must be reconsidered at room temperature). Thus, imposing this approximation, the system can be solved to obtain the spin injection efficiency,

$$P_j = \frac{R_F P_{\sigma F} + R_C P_G}{R_F + R_C + R_N} = \langle P_{\sigma} \rangle_R. \tag{2.26}$$

Spin injection efficiency is the conductivity spin polarization P_{σ} averaged over each region (remember that $P_{\sigma N} = 0$) and weighted by the corresponding effective resistance. Note that it does not depend on the current.

Spin accumulation at x = 0 from the N region (2.17) can be rewritten in terms of the spin injection efficiency,

$$\mu_{sN}(0) = -I\langle P_{\sigma}\rangle_R R_N. \tag{2.27}$$

Now, if $j < 0 \ (\Rightarrow)$, then electrons flow from F to N and $\mu_{sN}(0) > 0$; that is spin injection. If instead $j > 0 \ (\Leftarrow)$, electrons flow from N to F and $\mu_{sN}(0) < 0$; that is spin extraction. The latter is our case of interest.

2.1.2 Silsbee-Johnson Spin-Charge Coupling

In spin injection, driving spin-polarized electrons (due to magnetization) from F to N causes a non-equilibrium spin accumulation at N. In spin extraction, spin accumulation is generated in N at the interface with F; an emf appears in an open circuit, and current flows in a closed circuit. This is called Johnson-Silsbee spin-charge coupling [24, 25].

Considering once again an arrangement as in Fig. 2.1, with the new boundary condition that a non-equilibrium spin accumulation is sustained at the far right boundary of the nonmagnetic conductor,

$$\mu_{sN}(+\infty) \neq 0. \tag{2.28}$$

Meanwhile, spin relaxation at the ferromagnetic conductor causes spin to be in equilibrium at its far left boundary,

$$\mu_{sF}(-\infty) = 0. \tag{2.29}$$

Note that this is precisely the case in our CISS quantum circuit. There, spin accumulation at the far right boundary of the nonmagnetic conductor is sustained by the CISS effect.

The main goal is to find the induced emf under the condition of having an open circuit (j = 0),

$$emf = \mu_N(\infty) - \mu_F(-\infty). \tag{2.30}$$

It is necessary to introduce the concept of local charge neutrality. It refers to the condition where the net charge within a localized region is zero. To illustrate this, consider a Fermi gas in equilibrium, with an electron density n_0 and chemical potential η . When the gas is in a weakly non-equilibrium state in the presence of an electric field $E = -\nabla \phi$, and current is flowing, then

$$n_{\uparrow} = n_{\uparrow 0} (\eta + e\mu_{\uparrow} + e\phi) \approx n_{\uparrow 0} + \frac{\partial n_{\uparrow 0}}{\partial \eta} (e\mu_{\uparrow} + e\phi),$$
 (2.31)

$$n_{\downarrow} = n_{\downarrow 0} (\eta + e\mu_{\downarrow} + e\phi) \approx n_{\downarrow 0} + \frac{\partial n_{\downarrow 0}}{\partial \eta} (e\mu_{\downarrow} + e\phi),$$
 (2.32)

where for degenerate conductors, deviations from η are considered small; thus, the expansion is obtained. Also, for degenerate conductors and considering that E = 0,

$$\frac{\partial n_0}{\partial \eta} = g(\eta), \tag{2.33}$$

where $g(\eta)$ is the density of states per unit volume. Thus, considering this in both (2.31) and (2.32),

$$n_{\uparrow} = n_{\uparrow 0} + g_{\uparrow} e(\mu_{\uparrow} + \phi), \tag{2.34}$$

$$n_{\downarrow} = n_{\downarrow 0} + g_{\downarrow} e(\mu_{\downarrow} + \phi). \tag{2.35}$$

Thus, the total electron density is,

$$n = n_{\uparrow} + n_{\downarrow} = n_0 + eg(\mu + \phi) + eg_s\mu_s.$$
 (2.36)

Local charge neutrality condition implies that $n = n_0$, meaning that the additional charge contributions from μ , ϕ , and μ_s should collectively sum to zero. This condition eliminates

the electric field from the problem by relating it to the electrochemical potential [24],

$$g(\mu + \phi) + g_s \mu_s = 0, (2.37)$$

$$\phi(x) = -\mu(x) - P_q \mu_s(x), \tag{2.38}$$

where $P_g = g_s/g = (g_{\uparrow} - g_{\downarrow})/g$ is the spin polarization of the density of states. Since in the nonmagnetic conductor we have that $P_{gN} = 0$, we have for both the F and N regions, respectively,

$$\phi_F(x) = -\mu_F(x) - P_{aF}\mu_{sF}(x), \tag{2.39}$$

$$\phi_N(x) = -\mu_N(x). \tag{2.40}$$

Since $\mu_{sF}(-\infty) = 0$, then from (2.30)

$$\operatorname{emf} = -[\phi_N(\infty) - \phi_F(-\infty)] = -\Delta\phi. \tag{2.41}$$

Thus, the emf induced is equal to a voltage drop between the F and N regions. From the drift-diffusion model (well described in Reference [24]), the charge current is related to the gradient of electrochemical potential and spin accumulation,

$$\nabla \mu = \frac{1}{\sigma} (j - \sigma_s \nabla \mu_s) = \frac{1}{\sigma} j - P_\sigma \nabla \mu_s, \tag{2.42}$$

thus, considering that j=0 (open circuit) and that $P_{\sigma N}=0$

$$\nabla \mu_F = -P_{\sigma F} \nabla \mu_{sF}, \tag{2.43}$$

$$\nabla \mu_N = 0. \tag{2.44}$$

Integrating both equations over F $(-\infty,0)$ and N $(0,\infty)$ regions respectively and recalling that $\mu_{sF}(-\infty) = 0$

$$\mu_F(-\infty) - \mu_F(0) = P_{\sigma F} \mu_{sF}(0), \tag{2.45}$$

$$\mu_N(+\infty) - \mu_N(0) = 0. \tag{2.46}$$

As expected, the electrochemical potential across N is constant, while across F, there is an electrochemical potential drop due to the spin polarization of σ_F . Thus from (2.30),

$$\operatorname{emf} = \mu_N(\infty) - \mu_F(-\infty) = \Delta\mu(0) - P_{\sigma F}\mu_{sF}(0).$$
 (2.47)

The only thing that is left is finding expressions for $\Delta\mu(0)$ and $\mu_{sF}(0)$. From the equations of the current density at the contact, (2.20) and (2.21),

$$\Delta\mu(0) = -R_C P_G j_s(0) \tag{2.48}$$

and replacing it in (2.47) we have

$$emf = -\Delta\phi(0) = -R_C P_G I_s(0) - P_{aF} \mu_{sF}(0). \tag{2.49}$$

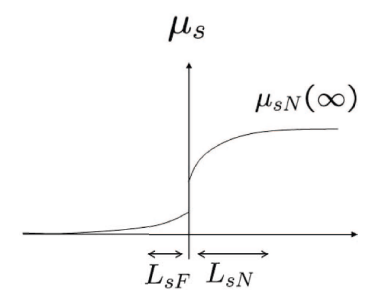


Figure 2.2: Spatial profile of the spin accumulation μ_s across the junction. The left side is the ferromagnetic conductor F, and the right is the nonmagnetic conductor N. From ref. [24].

Solving again the spin diffusion equation (2.4) with the new boundary conditions, the spatial profile of the spin accumulation in the nonmagnetic conductor at the contact is

obtained,

$$\mu_{sN}(x) = \mu_{sN}(\infty) + [\mu_{sN}(0) - \mu_{sN}(\infty)]e^{-x/L_{sN}}, \qquad (2.50)$$

$$\Rightarrow \nabla \mu_{sN}(0) = -\frac{1}{L_{sN}} [\mu_{sN}(0) - \mu_{sN}(\infty)], \tag{2.51}$$

where the value of $\mu_{sN}(0)$ is to be determined. On the other hand, for the ferromagnetic conductor, the spatial profile of $\mu_{sF}(x)$ has the same form as in (2.9); see Fig. 2.2. Thus, using these results and replacing them on (2.12), (2.14), and (2.22) considering that j = 0, the system of equations for the spin currents at x = 0 for each region is obtained,

$$j_{sN}(0) = -\frac{1}{R_N} [\mu_{sN}(0) - \mu_{sN}(\infty)], \qquad (2.52)$$

$$j_{sF}(0) = \frac{1}{R_F} \mu_{sF}(0), \tag{2.53}$$

$$j_{sC} = \frac{1}{R_C} \Delta \mu_s(0). \tag{2.54}$$

Just as before, it is assumed that spin current is conserved across the contact; thus,

$$j_{sN}(0) = j_{sF}(0) = j_{sC} \equiv j_s(0). \tag{2.55}$$

This allows to find the expression for $\Delta\phi(0)$, $\mu_{sF}(0)$, $j_s(0)$, and $\Delta\mu(0)$. Eliminating $j_s(0)$ and $\mu_{sN}(0)$ from (2.53), (2.52), and (2.54),

$$\mu_{sF}(0) = \frac{R_F}{R_F + R_C + R_N} \mu_{sN}(\infty). \tag{2.56}$$

Substituting it back on (2.53),

$$j_s(0) = \frac{1}{R_F + R_C + R_N} \mu_{sN}(\infty). \tag{2.57}$$

Replacing $j_s(0)$ on (2.48),

$$\Delta\mu(0) = -\frac{R_C P_G}{R_F + R_C + R_N} \mu_{sN}(\infty). \tag{2.58}$$

These results lead to the final expression for the emf. Replacing them on (2.49),

$$emf = -\frac{R_F P_{\sigma F} + R_C P_G}{R_F + R_C + R_N} \mu_{sN}(\infty) = -P_j \mu_{sN}(\infty).$$
 (2.59)

Recall that $P_j = \langle P_\sigma \rangle_R$ is the spin injection efficiency defined in (2.26). What equation (2.59) says is that when an equilibrium spin $(P_j, \text{ since it is the current polarization that we are injecting) is in electrical contact with a non-equilibrium spin, <math>\mu_{sN}(\infty)$, an emf is developed [24]. This effect allows the detection of non-equilibrium spin using a ferromagnetic conductor connected to the region containing this non-equilibrium spin. Measuring this emf gives away information about the spin accumulation in the nonmagnetic conductor [24].

Note that if $\mu_{sN}(\infty) > 0$ and the current spin polarization at the junction is positive, $P_j > 0$, then emf < 0. This, from (2.30), says that $\mu_F > \mu_N$ and, due to local charge neutrality, the opposite is true for electrostatic potential, $\phi_F < \phi_N$, thus electrons move from N to F.

2.2 Electron Transport in atomic-sized Contacts

According to Ohm's law, when a potential difference V is established between two points of a macroscopic conductor, a current I will flow through it that is related to the potential difference by the equation

$$V = IR, (2.60)$$

where R is the resistance to the flow of current across the conductor. Conductance G is defined as the opposite of resistance, being G = 1/R. From Drude's model, the expression of macroscopic conductance is obtained:

$$G = \sigma \frac{A}{L},\tag{2.61}$$

where σ is the conductivity that is an intensive property of the material, A is the cross-sectional area, and L is the conductor's length.

When the dimensions of the conductor shrink to the atomic scale, Ohm's law breaks down. In this regime, electrons transverse ballistically through the conductor since the distance they travel between two scattering events is much smaller than the atomic size.



Figure 2.3: Illustration of Landauer's representation of an electronic transport experiment. Left and right reservoirs with electrochemical potentials μ_L and μ_R , respectively, are connected to the sample by ideal one-dimensional leads.

If we consider two electron reservoirs L (left) and R (right) with electrochemical potentials μ_L and μ_R respectively. The reservoirs are connected through one-dimensional wires to a sample. Thus, the net current leaving the L lead (I_L) is given by the number of available electrons in the lead $N_L(\varepsilon)$, their velocity v_L , and transmission probability through the sample $T_{R,L}$ ($R \leftarrow L$) and the electrons that go into L should also be considered [26]. The net current is then

$$I_L = e \int d\varepsilon \left[T_{R,L} v_L \frac{1}{2} N_L(\varepsilon) f_L(\varepsilon) - T_{L,R} v_R \frac{1}{2} N_R(\varepsilon) f_R(\varepsilon) \right], \qquad (2.62)$$

where $N_i(\varepsilon) = 2/(hv_i)$ is the 1D density of states of the leads, $f_i(\varepsilon)$ is the Fermi-Dirac distribution of the charge carriers. Half of the density of states is taken because we only care for the outgoing states.

Assuming time-reversal for the transmission probabilities: $T_{R,L} = T_{L,R}$. The Fermi-Dirac distributions become a step-wise function at low temperatures: $f(\varepsilon) \to \Theta(\varepsilon_F - \mu_i)$. In the linear response regime, the integral is approximated by simply evaluating the transmission probabilities at ε_F . Thus, considering this and including a factor of 2 accounting for spin degeneracy, the current is

$$I_L = \frac{2e}{h} T_{R,L}(\mu_L - \mu_R),$$
 (2.63)

with $(\mu_L - \mu_R) = eV$, thus the two-probe conductance is given by

$$G_{R,L} = \frac{2e^2}{h} T_{R,L}. (2.64)$$

Finally, the conductance quantum is defined as $G_0 = 2e^2/h \approx 77.48\mu$ S. From this, the resistance of a 1D point contact can be calculated as $R_{G_0} = 1/G_0 \approx 12.9 \text{ k}\Omega$.

2.3 Transport Matrix Formalism

In this section, we describe coupled charge and spin transport in a circuit where a chiral component (either molecule, assembly of molecules, or solid-state chiral system) that generates a spin polarization due to CISS is connected to a ferromagnet (F) in two-terminal (2T) geometry to detect such spin accumulation generated in the chiral element as an emf due to the previously described Silsbee-Johnson spin-charge coupling. Each of these elements is characterized by a set of spin-dependent transmission and reflection probabilities. This set-up is used in CISS detection, where a magnetoresistance (MR) signal reveals the effect when changing the magnetization of the ferromagnetic electrode [10, 11]. The formalism is taken from the work of Yang, et al. [22, 23].

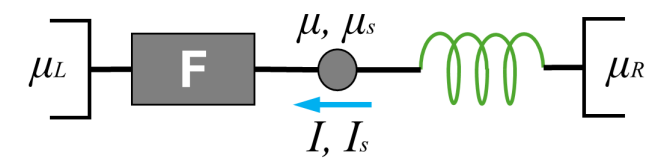


Figure 2.4: Generic 2T circuit containing a chiral component connected in series with a ferromagnet with a node in the middle. The bias voltage across the circuit is $\mu_L - \mu_R = -eV$. Currents from right to left (\Rightarrow) are taken as positive and negative from left to right (\Leftarrow). The chiral molecule is assumed to favor electrons with their spin parallel to their momentum. Adapted from ref. [22].

In this formalism, the chiral molecule is assumed to have time-reversal symmetry and spatial-inversion asymmetry that polarizes spin when charge current flows through it, allowing only one spin orientation to transmit. The exact description of how this takes place and the role of its spin-orbit coupling is outside the scope of this model. Hence, throughout this section, it is considered the molecule only allows the transmission of spins parallel to the electron's momentum; thus, instead of the usual \uparrow and \downarrow notation of spin direction that we have been using so far, we will switch to a \rightarrow and \leftarrow notation.

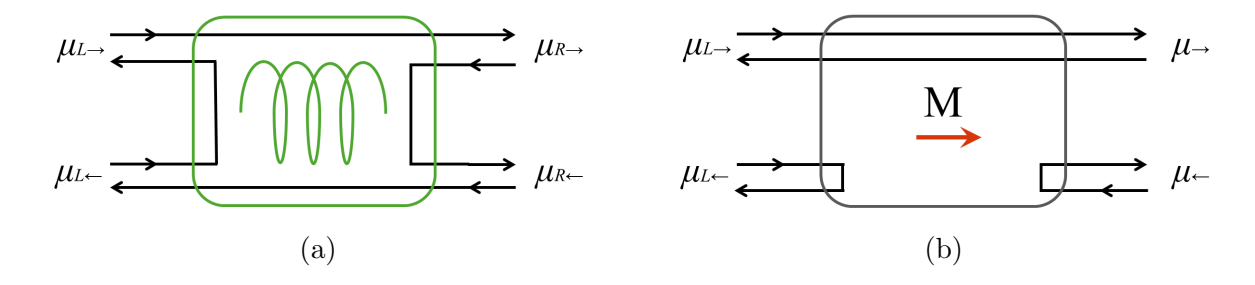


Figure 2.5: (a) Representation of ideal CISS effect. Directional spin transmission favors spin parallel to the electron's momentum while it flips and reflects the disfavored spin. Spin-specific electrochemical potentials are defined at both sides of the chiral component. Adapted from ref. [22] (b) Representation of a ferromagnetic conductor's spin-dependent transmission and reflection. Transmission is only allowed when the spin is aligned with the magnetization direction; otherwise, electrons are reflected. Adapted from ref. [27]

2.3.1 Spin-Charge Transport in the Chiral Component

First, it is necessary to define the spin-space transmission \mathbb{T} and reflection \mathbb{R} matrices in the chiral component represented in Fig. 2.5a. For the right-moving electrons,

$$\mathbb{T}_{\triangleright} = \begin{pmatrix} t_{\to \to} & t_{\longleftrightarrow} \\ t_{\to \leftarrow} & t_{\longleftrightarrow} \end{pmatrix}, \qquad \mathbb{R}_{\triangleright} = \begin{pmatrix} r_{\to \to} & r_{\longleftrightarrow} \\ r_{\to \leftarrow} & r_{\longleftrightarrow} \end{pmatrix}, \tag{2.65}$$

and for the left-moving, they are the time-reversed version of the right-moving ones,

$$\mathbb{T}_{\triangleleft} = \begin{pmatrix} t_{\leftarrow\leftarrow} & t_{\rightarrow\leftarrow} \\ t_{\leftarrow\rightarrow} & t_{\rightarrow\rightarrow} \end{pmatrix}, \qquad \mathbb{R}_{\triangleleft} = \begin{pmatrix} r_{\leftarrow\leftarrow} & r_{\rightarrow\leftarrow} \\ r_{\leftarrow\rightarrow} & r_{\rightarrow\rightarrow} \end{pmatrix}. \tag{2.66}$$

Using the Landuer-Buttiker formalism and considering the transmission and reflection matrices above, the current leaving each lead has the form,

$$\begin{pmatrix}
I_{R\to} \\
I_{R\leftarrow}
\end{pmatrix} = \frac{Ne}{h} \left[(\mathbb{I} - \mathbb{R}_{\triangleleft}) \begin{pmatrix} \mu_{R\to} \\ \mu_{R\leftarrow} \end{pmatrix} - \mathbb{T}_{\triangleright} \begin{pmatrix} \mu_{L\to} \\ \mu_{L\leftarrow} \end{pmatrix} \right],$$
(2.67)

$$\begin{pmatrix} I_{L\to} \\ I_{L\leftarrow} \end{pmatrix} = -\frac{Ne}{h} \left[(\mathbb{I} - \mathbb{R}_{\triangleright}) \begin{pmatrix} \mu_{L\to}, \\ \mu_{L\leftarrow} \end{pmatrix} - \mathbb{T}_{\triangleleft} \begin{pmatrix} \mu_{R\to} \\ \mu_{R\leftarrow} \end{pmatrix} \right], \tag{2.68}$$

where $I = I_{\rightarrow} + I_{\leftarrow}$ is the charge current, $I_s = I_{\rightarrow} - I_{\leftarrow}$ is the spin current, $\mu = (\mu_{\rightarrow} + \mu_{\leftarrow})/2$ is the (charge) electrochemical potential, and $\mu = (\mu_{\rightarrow} - \mu_{\leftarrow})/2$ is the spin accumulation as in the previous section [22, 24]. From equations (2.67) and (2.68), the transport matrix \mathcal{T}_c for the chiral system is

$$\begin{pmatrix}
I \\
-I_{sL} \\
I_{sR}
\end{pmatrix} = -\frac{Ne}{h} \begin{pmatrix} t & s & s \\
P_r r & \gamma_r & \gamma_t \\
P_t t & \gamma_t & \gamma_r \end{pmatrix} \begin{pmatrix} \mu_L - \mu_R \\
\mu_{sL} \\
\mu_{sR} \end{pmatrix}$$
(2.69)

where N is the number of spin-degenerate channels in the chiral molecule, e is the electron charge, h is the Planck constant and the matrix elements t, s, P_t , P_r , γ_t , and γ_r are all linear combinations of the directional transmission and reflection matrices, \mathbb{T} and \mathbb{R} , respectively. Elements t and r are the average transmission and reflection probabilities, respectively, P_t and P_r are the CISS-induced spin polarizations on the transmission and reflection probabilities, γ_t and γ_r describe spin relaxation and spin transport due to spin accumulation, and s is the charge current generated by the spin accumulation [22]. The

formalism treats spins separately, hence t + r = 2. Each of these quantities is defined as:

$$t = t_{\to\to} + t_{\to\leftarrow} + t_{\leftarrow\to} + t_{\leftarrow\leftarrow}, \tag{2.70}$$

$$r = r_{\to\to} + r_{\to\leftarrow} + r_{\leftarrow\to} + r_{\leftarrow\leftarrow}, \tag{2.71}$$

$$\gamma_t = t_{\to \to} - t_{\to \leftarrow} - t_{\leftarrow \to} + t_{\leftarrow \leftarrow}, \tag{2.72}$$

$$\gamma_r = r_{\to \to} - r_{\to \leftarrow} - r_{\leftarrow \to} + r_{\leftarrow \leftarrow} - 2, \tag{2.73}$$

$$P_t = (t_{\to \to} - t_{\to \leftarrow} + t_{\leftarrow \to} - t_{\leftarrow \leftarrow})/t, \tag{2.74}$$

$$P_r = (r_{\to \to} - r_{\to \leftarrow} + r_{\leftarrow \to} - r_{\leftarrow \leftarrow})/r, \tag{2.75}$$

$$s = t_{\rightarrow \rightarrow} + t_{\rightarrow \leftarrow} - t_{\leftarrow \rightarrow} - t_{\leftarrow \leftarrow} \tag{2.76}$$

$$= -r_{\rightarrow \rightarrow} - r_{\rightarrow \leftarrow} + r_{\leftarrow \rightarrow} + r_{\leftarrow \leftarrow}. \tag{2.77}$$

Symmetries are of central importance in solid-state physics. Time-reversal symmetry refers to microscopic systems that remain unchanged under a time-reversal operation \hat{T} . Macroscopic systems follow thermodynamics, and thus, most processes are irreversible. Onsager showed that in the linear response regime (small perturbations around thermodynamic equilibrium), these processes are subject to constraints imposed by time-reversal symmetry [23]. Onsager reciprocity relations in the linear regime require that under time-reversal (that is, magnetization and magnetic field reversal), the transport matrix satisfies $\mathcal{T}_{ij}(H,M) = \mathcal{T}_{ji}(-H,-M)$. Considering Onsager reciprocity on \mathcal{T}_c gives that $P_t t = P_r r = s$, and therefore it follows Onsager reciprocity by being symmetric [23, 22]. Connecting the chiral component to the left reservoir as depicted in Fig. 2.4, $\mu_{sL} = 0$ and \mathcal{T} reduces to a 2 × 2 matrix concerned only on its left interface with the node,

$$\begin{pmatrix} I \\ -I_s \end{pmatrix} = -\frac{Ne}{h} \begin{pmatrix} t & P_t t \\ P_t t & \gamma_r \end{pmatrix} \begin{pmatrix} \mu_L - \mu_R \\ \mu_s \end{pmatrix}. \tag{2.78}$$

. The matrix can be written in terms of just P_t rewriting γ_t and γ_r ,

$$\gamma_t = -t + \frac{P_t t + s}{\eta_t} = -\frac{1 + 2P_t}{\eta_t} t, \tag{2.79}$$

$$\gamma_r = -t + \frac{P_r r + s}{\eta_r} = -\frac{1 + 2P_t}{\eta_r} t, \tag{2.80}$$

where η_t and η_r are defined as,

$$\eta_t = \frac{t_{\to \to} - t_{\leftarrow \leftarrow}}{t_{\to \to} + t_{\leftarrow \leftarrow}},\tag{2.81}$$

$$\eta_r = \frac{r_{\to\to} - r_{\leftarrow\leftarrow}}{r_{\to\to} + r_{\leftarrow\leftarrow}}.$$
 (2.82)

2.3.2 Spin-Charge Transport in the achiral Ferromagnetic Tunnel Junction (FMTJ)

The ferromagnet (F) breaks time-reversal symmetry, and spin accumulation is zero inside it since spin relaxation is strong [22]. The ferromagnetic tunnel junction (FMTJ) provides a spin polarization to any out-flowing current. This polarization is defined as $P_F = (G_{\rightarrow} - G_{\leftarrow})/(G_F)$, where $G_{\rightarrow(\leftarrow)}$ is the spin-specific conductance and $G_F = G_{\rightarrow} + G_{\leftarrow}$ is the total conductance. When a spin accumulation is formed at the interface, the FMTJ generates a charge voltage [24]. Considering that the FMTJ is connected to a reservoir on its left, the only concern is at its right interface with the node in Fig. 2.4. The spin-specific currents on the left side are given by:

$$I_{\to} = -\frac{1}{e}G_{\to} \left[\mu_L - (\mu_R + \mu_{sR})\right],$$
 (2.83)

$$I_{\leftarrow} = -\frac{1}{e}G_{\leftarrow} \left[\mu_L - (\mu_R - \mu_{sR})\right].$$
 (2.84)

Defining a transmission coefficient $0 \leq T \leq 2$, the transport matrix \mathcal{T}_{FC} is therefore

$$\begin{pmatrix} I \\ I_s \end{pmatrix} = -\frac{N'e}{h} \begin{pmatrix} T & -P_F T \\ P_F T & -T \end{pmatrix} \begin{pmatrix} \mu_L - \mu_R \\ \mu_s \end{pmatrix}. \tag{2.85}$$

where N' is the number of spin-degenerate channels. \mathcal{T}_F satisfies Onsager reciprocity relations on the linear regime by being antisymmetric because a reversal on the magnetization M corresponds to a sign change of P_F [22, 23].

2.3.3 Spin-Charge Transport in 2T geometry

Now, a circuit geometry of two terminals (2T) is considered, as shown in Fig. 2.4. Both transport matrix equations (2.78) and (2.85) can be rewritten into conductance matrix equations. Thus, for the chiral component, the elements of the conductance matrix are

$$g_1 = \frac{Ne^2}{h}t, (2.86)$$

$$g_2 = \frac{Ne^2}{h} P_t t = g_3, (2.87)$$

$$g_4 = -\frac{Ne^2}{h} \left(1 + \frac{2P_t}{\eta_r} \right) t. {(2.88)}$$

Note that $g_2 = g_3$ results from the matrix being symmetric due to Onsager reciprocity. For the FMTJ, the elements of its conductance matrix are

$$G_1 = \frac{N'e^2}{h}T, (2.89)$$

$$G_2 = -\frac{N'e^2}{h}P_F T = -G_3, (2.90)$$

$$G_4 = -\frac{-N'e^2}{h}T. (2.91)$$

Here $G_2 = -G_3$ because of the matrix being antisymmetric. Thus, the conductance matrices for the chiral component and the FMTJ are

$$\begin{pmatrix} I \\ -I_s \end{pmatrix} = -\frac{1}{e} \begin{pmatrix} g_1 & g_2 \\ g_3 & g_4 \end{pmatrix} \begin{pmatrix} \mu - \mu_R \\ \mu_s \end{pmatrix}, \tag{2.92}$$

$$\begin{pmatrix} I \\ -I_s \end{pmatrix} = -\frac{1}{e} \begin{pmatrix} G_1 & G_2 \\ G_3 & G_4 \end{pmatrix} \begin{pmatrix} \mu_L - \mu \\ \mu_s \end{pmatrix}, \tag{2.93}$$

There are no L or R subscripts in the currents (charge and spin) because, in the steady state, both I and I_s should be equal on both sides of the node. Therefore, (2.92) and (2.93) describe the currents at both sides of the node. This allows to write the expressions for I, μ , and μ_s as a function of the 2T bias $\mu_L - \mu_R$

$$\mu_s = \frac{G_3 g_1 + G_1 g_3}{f} (\mu_R - \mu_L), \tag{2.94}$$

$$\mu = \mu_L - \frac{g_3^2 + G_3 g_3 - g_1 (G_4 + g_4)}{f} (\mu_r - \mu_R), \tag{2.95}$$

$$= \mu_R + \frac{-G_3^2 - G_3 g_3 - G_1 (G_4 + g_4)}{f} (\mu_R - \mu_L), \tag{2.96}$$

$$I = -\frac{1}{e} \frac{G_1 g_3^2 - g_1 G_3^2 - G_1 g_1 (G_4 + g_4)}{f} (\mu_R - \mu_L), \tag{2.97}$$

$$f = g_3^2 - G_3^2 - (G_1 + g_1)(G_4 + g_4). (2.98)$$

Note that f does not change with either chirality or magnetization reversal since it has a second-order dependence on g_3 and G_3 that depend on the CISS-induced spin polarization of the transmitted electrons, P_t , and on the spin polarization of the out-flowing current at the ferromagnet, P_t respectively. Charge current I depends on g_3^2 and G_3^2 , remaining invariant under both reversals. Consequently, the 2T conductance is invariant under both asymmetries reversals in the linear response,

$$G_{2T} = \frac{G_1 g_3^2 - g_1 G_3^2 - G_1 g_1 (G_4 + g_4)}{f} = G_{2T}(P_F^2, P_t^2). \tag{2.99}$$

Because of this, no MR signal should be measured from the edges in the 2T geometry. This is in agreement with what Onsager reciprocity relations, which state that in the linear response regime, 2T conductance remains constant under either magnetization M or magnetic field H reversal [23],

$$G_{ij}(H, M) = G_{ij}(-H, -M).$$
 (2.100)

However, μ and μ_s are affected by both asymmetries, having a first-order dependence on g_3 and G_3 .

The reason why MR vanishes in 2T geometry can be understood as two opposite processes that cancel each other out in the linear regime. First, due to CISS, spin is injected and a spin accumulation forms at the node that is detected at the ferromagnet as a charge voltage due to Silsbee-Johnson spin-charge coupling [24]. This indeed changes when the ferromagnet magnetization is reversed. In the second process, the ferromagnet now injects spin into the chiral molecule, and due to Onsager reciprocity, it is detected as charge voltage.

Yang et al. propose that for MR signals to be measured, an energy relaxation process is needed inside the device. In Reference [21], Yang et al. also show that it is possible to measure such MR in the linear regime if the geometry is of more than two terminals.

2.4 Tight-Binding Example Model of the Electronic Transport Through a Chiral Molecule

As seen in the previous section, the transport matrix of the chiral component is defined by spin-dependent transmission and reflection coefficients. These coefficients can be obtained by carrying out a quantum description of the transport through the chiral component. To show how this can be done, we present a simple example of a tight-binding model of electron transport. We consider three sites in a helical structure, each with two orbitals, p_x and p_z . This helix is connected to two leads composed of semi-infinite chains of p_x orbitals.

The helix has a radius a, a pitch b, and the angle between two contiguous atoms is $\Delta \phi = \phi_m - \phi_n$. We will use cylindrical coordinates, with the helix resting on the XY plane. For simplicity, we will consider that our atoms are positioned at every half turn, that is $\Delta \phi = \pi$, with the first atom at the bottom with $\phi_1 = 0$ and the last at b with

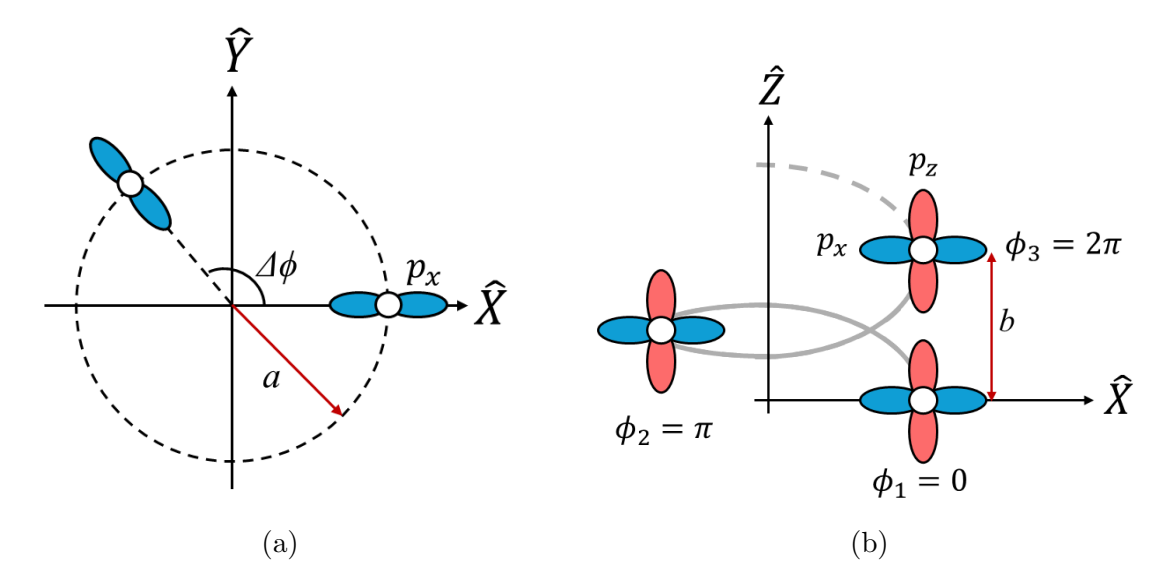


Figure 2.6: Structure of the example model for the molecule in (a) the XY plane, showing the p_x orbitals; (b) in the XZ plane, showing the positions of the three sites in the model and the p_z orbitals.

 $\phi_3 = 2\pi$. We define the position vector at site n as,

$$\mathbf{R}_n = a \left(\cos \phi_n \hat{X} + \sin \phi_n \hat{Y} + \frac{b\Delta\phi}{2\pi} \hat{Z} \right). \tag{2.101}$$

To build the TB Hamiltonian, Following the model of Ref. [17], we must consider all possible interactions between orbitals in the same atom and different atoms. The spin transport is defined by the Hamiltonian:

$$\mathcal{H} = \mathcal{H}_0 + \mathcal{H}_{lead}, \tag{2.102}$$

where $\mathcal{H}_0 = \mathcal{H}_{TB} + \mathcal{H}_{SO}$. \mathcal{H}_{TB} is the TB Hamiltonian on the Slater-Koaster scheme that describes the overlaps between nearest neighbors' orbitals.

We will consider that the only interaction between orbitals in the same atom is intrinsic spin-orbit coupling, given by the Hamiltonian:

$$\mathcal{H}_{SO} = -\frac{1}{r} \frac{\partial V}{\partial r} \frac{e}{2m_0^2 c^2} \mathbf{L} \cdot \mathbf{S},$$

$$= \lambda \mathbf{L} \cdot \mathbf{S},$$
(2.103)

where V is the atomic potential, m_0 is the effective electron mass, $\mathbf{L} = \mathbf{r} \times \mathbf{p}$ is the orbital angular momentum operator, and \mathbf{S} is the spin angular momentum operator. In the $|l, m_l\rangle$ basis, we can write the p_x and p_z orbitals as,

$$|p_x\rangle = -\frac{1}{\sqrt{2}}(|1,1\rangle - |1,-1\rangle),$$
 (2.104)

$$|p_z\rangle = |1,0\rangle. \tag{2.105}$$

Therefore, the matrix elements of the spin-orbit Hamiltonian are given by,

$$\mathcal{H}_{SO} = \begin{array}{c|cc} \hline & |p_x\rangle & |p_z\rangle \\ \hline \langle p_x| & 0 & i\mathbf{S}_y\xi_p \\ \langle p_z| & -i\mathbf{S}_y\xi_p & 0 \\ \end{array}$$

where $\xi_p = \lambda \hbar^2/2$ and \mathbf{S}_y is given by

$$\mathbf{S}_{v_n} = -\mathbf{S}_X \sin \phi_n + \mathbf{S}_Y \cos \phi_n, \tag{2.106}$$

where \mathbf{S}_Y is the Pauli matrix representing the electron spin degree of freedom in the Z axis. Using the Slater-Koaster scheme as in Ref. [17], the overlap between the orbitals μ_n and μ_m at site n and m respectively, are given by

$$E_{\mu_n\mu_m}^{nm} = \langle \mu_n | V | \mu_m \rangle$$

$$= (\hat{\mathbf{n}}(\mu_n) \cdot \hat{\mathbf{n}}(\mu_m)) V_{\mu_n\mu_m}^{\pi} + \frac{(\mathbf{R}_{nm} \cdot \hat{\mathbf{n}}(\mu_n))(\mathbf{R}_{nm} \cdot \hat{\mathbf{n}}(\mu_m))}{|\mathbf{R}_{mn}|^2} (V_{\mu_n\mu_m}^{\sigma} - V_{\mu_n\mu_m}^{\pi}),$$
(2.107)

where $\mathbf{R}_{mn} = \mathbf{R}_m - \mathbf{R}_n$, $\hat{\mathbf{n}}(\mu_n)$ is the unit vector along the μ_n orbital direction, and $V_{\mu_n\mu_m}^{\pi,\sigma}$ are the Slater-Koaster π and σ overlaps [17].

With our example model configuration, we have

$$\hat{\mathbf{n}}(x_n) = \cos \phi_n \hat{\mathbf{X}} + \sin \phi_n \hat{\mathbf{Y}}, \qquad (2.108)$$

$$\hat{\mathbf{n}}(z_n) = \hat{\mathbf{Z}},\tag{2.109}$$

and the vector \mathbf{R}_{mn} joining the two atoms is

$$\mathbf{R}_{mn} = 2a \left[-\sin\left(\frac{\phi_m + \phi_n}{2}\right) \sin\frac{\Delta\phi}{2}\hat{\mathbf{X}} + \cos\left(\frac{\phi_m + \phi_n}{2}\right) \sin\frac{\Delta\phi}{2}\hat{\mathbf{Y}} + \frac{b\Delta\phi}{2\pi}\hat{\mathbf{Z}} \right]. \quad (2.110)$$

With this in mind and considering $\phi_1 = 0$, $\phi_2 = \pi$, and $\phi_3 = 2\pi$ with $\Delta \phi = \pi$, we obtain the Slater-Koaster overlaps,

$$E_{xx}^{nm} = -V_{pp}^{\pi} - \frac{V_{pp}^{\sigma} - V_{pp}^{\pi}}{1 + b^2/4},$$
(2.111)

$$E_{zz}^{nm} = V_{pp}^{\pi} + \frac{b^2(V_{pp}^{\sigma} - V_{pp}^{\pi})}{16a^2(1 + b^2/4)},$$
(2.112)

$$E_{zx}^{nm} = \frac{b(V_{pp}^{\sigma} - V_{pp}^{\pi})}{2a(1 + b^2/4)}.$$
 (2.113)

Note that if b = 0, there's no overlap between p_x and p_z . With this result and considering the SO Hamiltonian \mathcal{H}_{SO} , we can write the TB Hamiltonian of the three-site-model helix \mathcal{H}_0 :

$$\mathcal{H}_{0} = \mathcal{H}_{TB} + \mathcal{H}_{SO} = \begin{vmatrix} |p_{x_{1}}\rangle & |p_{z_{1}}\rangle & |p_{z_{1}}\rangle & |p_{z_{2}}\rangle & |p_{z_{3}}\rangle & |p_{z_{3}}\rangle \\ |p_{x_{1}}\rangle & \varepsilon_{p} & i\mathbf{S}_{y}\xi_{p} & E_{xx}^{12} & E_{xx}^{12} & 0 & 0 \\ |\langle p_{z_{1}}\rangle & -i\mathbf{S}_{y}\xi_{p} & \varepsilon_{p} & -E_{xx}^{12} & E_{zz}^{12} & 0 & 0 \\ |\langle p_{x_{1}}\rangle & E_{xx}^{21} & E_{xx}^{21} & E_{xx}^{21} & \varepsilon_{p} & i\mathbf{S}_{y}\xi_{p} & E_{xx}^{23} & E_{xx}^{23} \\ |\langle p_{x_{2}}\rangle & -E_{xz}^{12} & E_{zz}^{12} & -i\mathbf{S}_{y}\xi_{p} & \varepsilon_{p} & -E_{xz}^{23} & E_{zz}^{23} \\ |\langle p_{x_{3}}\rangle & 0 & 0 & E_{xx}^{32} & E_{xz}^{32} & \varepsilon_{p} & i\mathbf{S}_{y}\xi_{p} \\ |\langle p_{z_{3}}\rangle & 0 & 0 & -E_{xz}^{32} & E_{zz}^{32} & -i\mathbf{S}_{y}\xi_{p} & \varepsilon_{p} \end{vmatrix}$$

Note that because of the spin degree of freedom, the Hamiltonian matrix is 12×12 . We still have to connect the helix to the leads composed of semi-infinite p_x orbitals; the overlaps between them and the helix sites 1 and 2 are purely kinetic terms. The self-energies of each lead are given by [26]

$${}^{L}\Sigma_{1} = {}^{L}\Delta_{1} - i {}^{L}\Gamma_{1} = \left| \frac{{}^{L}V_{pp}^{\pi}}{{}^{0}V_{pp}^{pi}} \right|^{2} \left(\frac{\varepsilon - \varepsilon_{p}^{0}}{2} + i \sqrt{({}^{0}V_{pp}^{\pi})^{2} - \frac{(\varepsilon - \varepsilon_{p}^{0})^{2}}{4}} \right), \tag{2.114}$$

$${}^{R}\Sigma_{3} = {}^{R}\Delta_{3} - i\,{}^{3}\Gamma_{3} = \left|\frac{{}^{R}V_{pp}^{\pi}}{{}^{0}V_{pp}^{pi}}\right|^{2} \left(\frac{\varepsilon - \varepsilon_{p}^{0}}{2} + i\sqrt{({}^{0}V_{pp}^{\pi})^{2} - \frac{(\varepsilon - \varepsilon_{p}^{0})^{2}}{4}}\right),\tag{2.115}$$

where ${}^{L,R}V^{\pi}_{pp}$ are the overlaps of the p_x orbitals between the first and third site in helix, and the left and right lead, respectively, ${}^{0}V^{\pi}_{pp}$ is the overlap of the p_x orbitals inside the leads, and ε^0_p is the energy of the p orbitals in the lead. The lead Hamiltonian is

$$\mathcal{H}_{\text{lead}} = {}^{L}\Sigma_{1}|p_{z_{1}}\rangle\langle p_{z_{1}}| + {}^{R}\Sigma_{3}|p_{z_{3}}\rangle\langle p_{z_{3}}|. \tag{2.116}$$

Considering this and the TB Hamiltonian, we can write the complete Hamiltonian \mathcal{H} for the system coupled to the leads, summarized in the table below.

The Green function is given by,

$$G^{(R)} = [\varepsilon I - \mathcal{H}]^{-1}. \tag{2.117}$$

where R stands for retarded. From the obtained 12×12 Green matrix and the Fisher and Lee formula [26], we can relate it to the spin-specific transmission between the leads as

$$T_{3,1}^{\uparrow\uparrow}(\varepsilon) = 4^L \Gamma_1(\varepsilon) G_{p_{z_3\uparrow}, p_{z_1\uparrow}}^R(\varepsilon)^R \Gamma_3(\varepsilon) G_{p_{z_1\uparrow}, p_{z_3\uparrow}}^A(\varepsilon), \tag{2.118}$$

$$T_{3,1}^{\downarrow\downarrow}(\varepsilon) = 4^L \Gamma_1(\varepsilon) G_{p_{2,\downarrow},p_{2,\downarrow}}^R(\varepsilon) {}^R \Gamma_3(\varepsilon) G_{p_{2,\downarrow},p_{2,\downarrow}}^A(\varepsilon), \qquad (2.119)$$

$$T_{3,1}^{\uparrow\downarrow}(\varepsilon) = 4^L \Gamma_1(\varepsilon) G_{p_{z_3\uparrow}, p_{z_1\downarrow}}^R(\varepsilon)^R \Gamma_3(\varepsilon) G_{p_{z_1\downarrow}, p_{z_3\uparrow}}^A(\varepsilon), \qquad (2.120)$$

$$T_{3,1}^{\downarrow\uparrow}(\varepsilon) = 4^L \Gamma_1(\varepsilon) G_{p_{z_3\downarrow}, p_{z_1\uparrow}}^R(\varepsilon)^R \Gamma_3(\varepsilon) G_{p_{z_1\uparrow}, p_{z_3\downarrow}}^A(\varepsilon), \tag{2.121}$$

with these being equivalent to $t_{\to\to}$, $t_{\leftarrow\leftarrow}$, $t_{\to\leftarrow}$, and $t_{\leftarrow\to}$ in the transport matrix formalism. The correspondent reflection probabilities r are found by simply considering the elements of the Green matrix of the same site, that is, $G_{p_{z_n},p_{z_n}}^R$ and $G_{p_{z_n},p_{z_n}}^A$.

Chapter 3

Toward Transport in Nanoscale structures: Experimental Set-up

3.1 Mechanically Controlled Break Junction

We used a mechanically controlled break junction (MCBJ) set-up to study electron transport through atomic-sized contacts. The device consists of a clamp of two brass pieces that will hold the sample placed onto a flexible substrate with the pressure exerted by four nuts at the top. A piezo stack (Thorlabs PK3JMAP1) is placed on a third brass piece that is moved up and down by a micrometer screw. Thus, the set-up works as a three-point bending mechanism that bends the flexible substrate with the action of the piezo. A diagram and picture of the MCBJ are shown in Fig. 3.1a and 3.1b, respectively.

The most common choice for the flexible substrate in literature is a plate of phosphorous bronze about 1 mm thick, which is covered with an insulating film, usually Kapton [28, 29, 30]. Instead, we decided to design 3D-printable PLA flexible substrates, reducing the costs and complexity of the sample preparation. The printed pieces were 26×6 mm and 1 mm thick, with the middle section reduced to half the thickness to ensure a higher

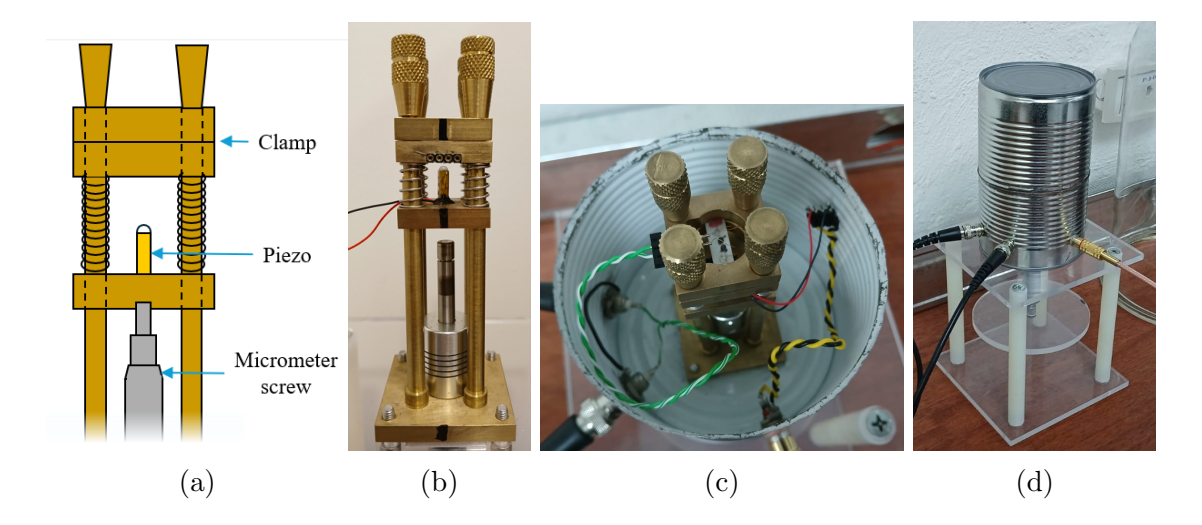


Figure 3.1: (a) Diagram of the MCBJ set-up. The clamp comprises two brass pieces that hold the flexible substrate in place. The micrometer screw moves the piezo up close to the substrate. (b) Picture of the real set-up, donated by the Laboratory of Molecular Electronics, Yachay Tech. (C) and (d) show the MCBJ inside its metal enclosure for noise reduction.

flexibility. Aside from costs, the advantage is that Kapton is no longer needed to insulate the sample from the substrate, and we can prepare many substrates in less than an hour.

To reduce electromagnetic noise and interference, we placed the electronics inside an aluminum enclosure, and so was the MCBJ, as seen in Fig. 3.1c and 3.1d. Coaxial cables were also used to connect everything in the set-up.

This set-up was used to study electron transport in atomic-sized contacts with homometallic (Au-Au) and bimetallic junctions (Au-Ni) at ambient temperature. In both cases, conductance (current) traces were measured and analyzed statistically, building histograms from thousands of traces.

3.2 Electronics

The MCBJ is connected to a set of electronics that serves three functions: constant voltage supply for the junction, current-to-voltage converter and amplifier, and trigger for the data

acquisition. Fig. 3.2 shows the entire circuit used for the equipment operation. All the electronics are powered by a symmetric $V_{cc} = \pm 10$ V source.

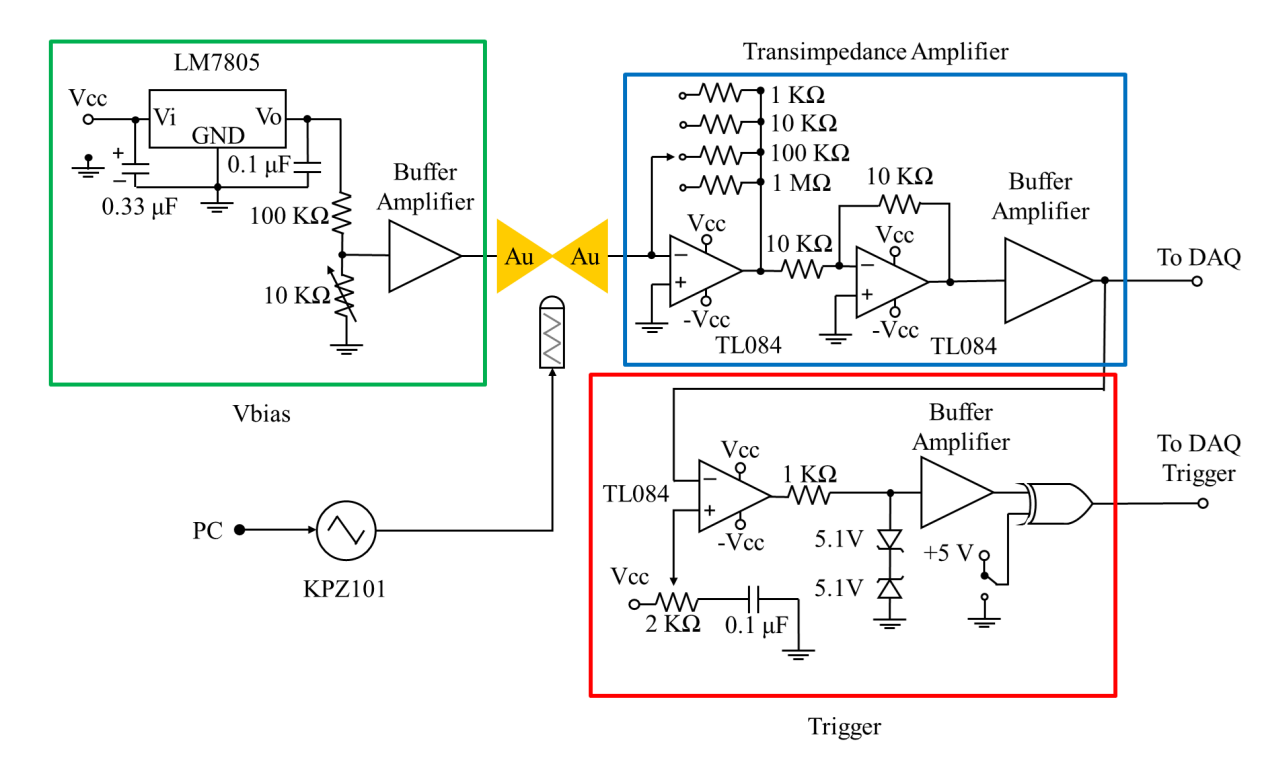


Figure 3.2: Circuit diagram of the electronics connected to the MCBJ. Enclosed in green is the bias voltage circuit that provides a constant supply of $V_{\rm bias} = 200$ mV. Enclosed in blue the trans-impedance amplifier circuit is enclosed in blue that converts the output current from the junction into an amplified voltage signal. Enclosed in red is the trigger circuit that compares the output voltage signal from the trans-impedance amplifier to a selected reference voltage. Depending on whether the signal exceeds or not said reference, it sends a pulse to the trigger input in the DAQ. The piezo is controlled by Thorlabs KPZ101, which sends a 100 V triangular signal.

In the bias voltage circuit, LM7805 sends out a constant 5 V. Then, a voltage divider with a variable resistor controls the bias voltage for the break junction. We used $V_{\text{bias}} = 200 \text{ mV}$, to prevent electric noise. When this signal passes through the Au-Au junction, a small current comes out. The trans-impedance amplifier circuit converts this current to an amplified voltage signal. This is done by the TL084 op-amp connected to the selected feedback resistor R_f that determines the amplification factor from 10^3 to 10^5 . The output signal then goes to the analog input of the Digilent MCC USB-1208HS DAQ device.

To activate the trigger, the circuit compares the trans-impedance amplifier output V_0 with a controllable reference voltage. When the voltage is higher than the reference, the



Figure 3.3: Aluminum enclosure of the electronics of the MCBJ device depicted on Figure 3.2. The knob allows the amplification selection. The red LED indicates the action of the trigger circuit.

output from the op-amp will saturate to $+V_{cc}$, and $-V_{cc}$ if it is lower (in fact, it will saturate to $\sim \pm 8.529$ V). This value is then compared in an XOR gate with either 5 V or ground. When the selector is at ground, then the output will be high if $V_0 > V_{ref}$ and low otherwise. If instead the selector is at 5 V, then the opposite occurs; the output is high if $V_0 < V_{ref}$ and low otherwise. In this study, the latter is used with $V_{ref} \approx V_{cc}$, such that the trigger activates when the voltage signal drops from V_0 .

A controlled high-voltage signal is sent to the piezo element to bend the substrate. For this purpose, we use Thorlabs KPZ101 K-Cube Piezo Controller, which automatically controls the piezo element up to 1 kHz. PC-controlled operation is done with LabVIEW utilizing the device's control software package, Kinesis. The LabVIEW program sends positive DC voltage ramps (triangular functions) from KPZ101 to the piezo stack (Thorlabs PK3JMAP1). The ramps cause repeated elongation and contraction of the piezo, which bends the substrate, breaking and forming the atomic-size contacts between both tips of the electrodes.

3.3 Homometallic Junctions

To make the homometallic sample, we used a 0.1mm diameter 4N purity (99.99%) Au. Electrodes were formed by making a notch using a 3D-printed device that consisted of a scalpel blade whose altitude was mechanically controlled by a micrometer screw. Spring kept the back of the scalpel under pressure to ensure continuous contact between the blade and the micrometer. The device is as shown in Figure 3.4b. Several tries were needed to obtain the desired notch with a proper depth.

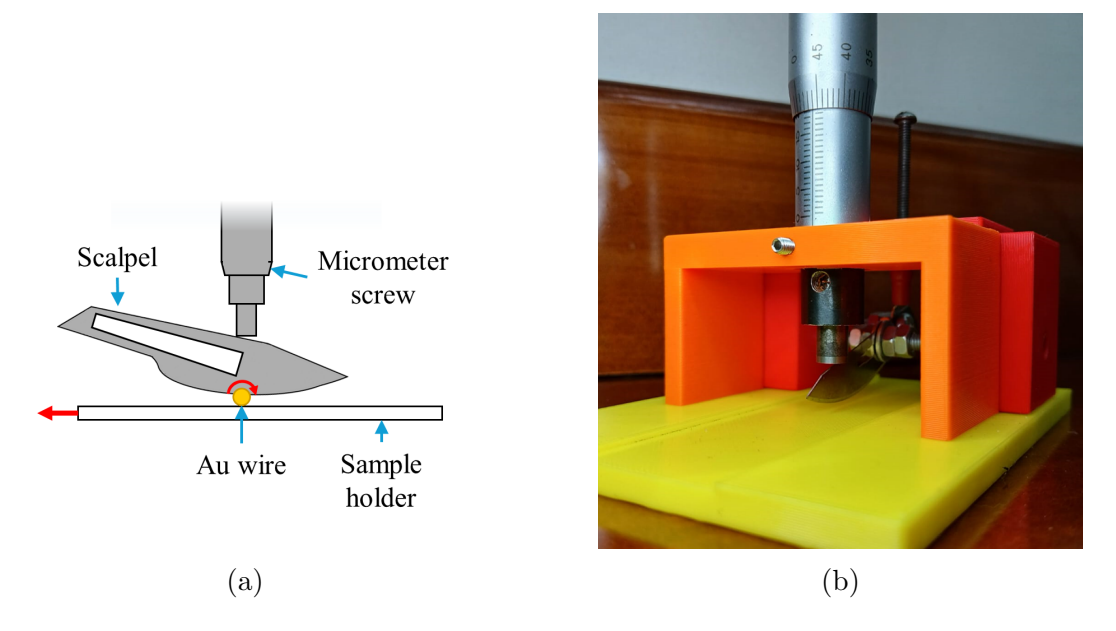


Figure 3.4: Notching mechanism for the preparation of homometallic junction samples. (a) Diagram of the notching process for the homometallic junction samples. (b) 3D printed PLA device for notching the sample wires.

This sample was placed in a PLA flexible substrate. To prefix the sample, nail polish drops were placed at its ends. Then, after letting it dry, epoxy adhesive drops were placed near the junction, and by allowing them to cure for a few minutes, they were gently spread to reach the start of the notch. This final fix was left inside a protective glass enclosure for 24 hours to cure fully. Once the curing process was done, two thin copper probes (roughly the same diameter as the Au wire) were attached to the sample, covering the spot with silver paint to enhance electrical contact. The sample is loaded onto the MCBJ, with the clamp holding the flexible substrate in place.

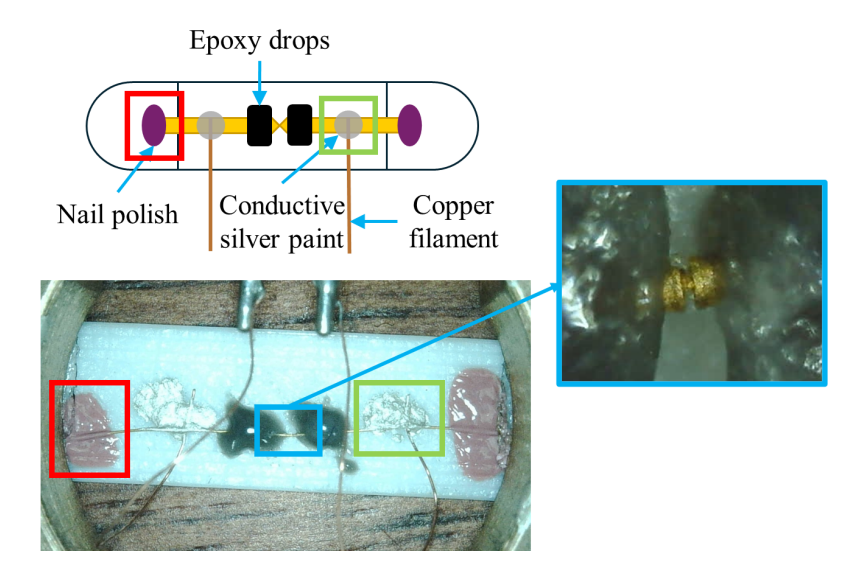


Figure 3.5: Sample placed on the PLA flexible substrate. A diagram can be seen in the upper part, while a picture of the real montage can be seen in the lower part.

The flexible substrate bends under the displacement of the piezo, stretching the wire and breaking the notch. Then, the piezo contracts, and the substrate returns to its natural form, squeezing the electrode tips back together and re-forming the contact. This rupture and junction formation was done continuously. Since no two traces are equal because of contamination, thermal interaction, electromagnetic noise, contact structure, etc., hundreds of contact rupture traces were measured.

3.4 Bimetallic Samples

With the same MCBJ set-up previously described, bimetallic junctions can also be studied, which are junctions where the electrodes are made of different metals. Considering that some metals have the habitability to wet others [29, 31], we chose Au and Ni, where the former wets the latter. This is convenient since we want to replicate the set-ups used in the literature of CISS in further studies. Thus, it requires generating a magnetization on the ferromagnet (Ni) so spin selection can be measured in I-V curves.

The technique used is described by Tal et al. [29], where studied bimetallic samples of diverse materials including Au-Ni in a vacuum chamber at 4.2 K. The idea is that the

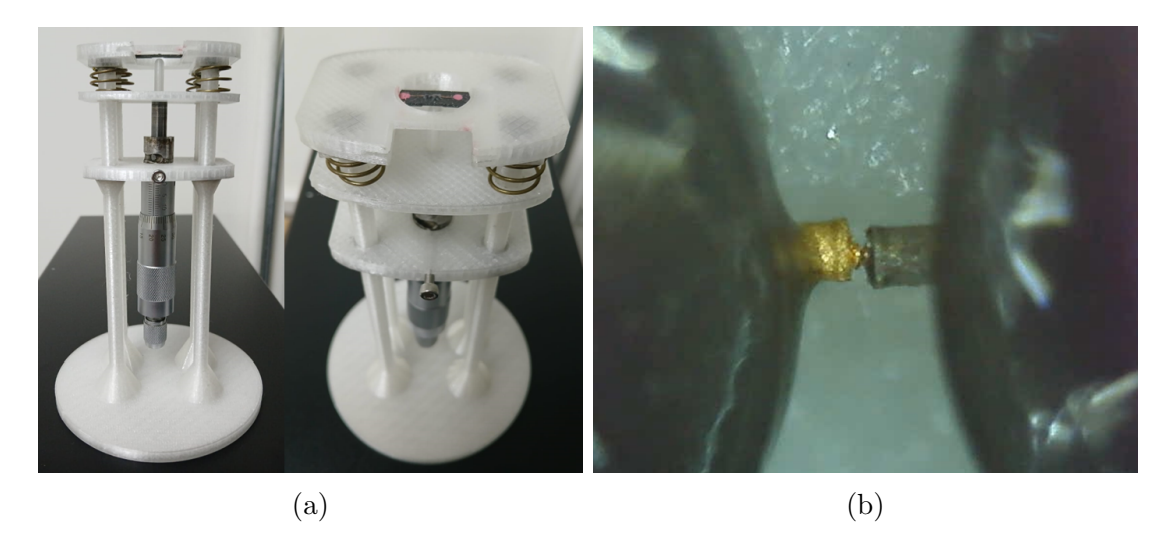


Figure 3.6: (a) Three-point bending device for the bimetallic junction sample preparations. With the micrometer screw, the device keeps the flexible substrate slightly bent, allowing us to align the wires on top of it with their tips in contact. After relaxation of the substrate, the tips squeeze against each other, forming a larger contact. (b) Bimetallic sample of Au-Ni obtained by this method.

flexible substrate must be kept bent while the sample is prepared. Therefore, an adjustable three-point bending device was 3D printed, as seen in Figure 3.6a. The amount of bending done must be small, considering that the action of the piezo in the MCBJ device is of the order of micrometers. Both sample wires were cut with a sharp tip at one end and placed on the bent substrate. The same notching mechanism was used for this sharpening, but this time, instead of calibrating the blade height such that just a notch was made, it was lowered until it cut through the wire, leaving little tips on each end.

Under a stereoscopic microscope, one of the wires is attached to the substrate with a drop of nail polish on its back end. The second wire is then attached the same way, ensuring its tip's alignment with that of the first one. After the nail polish cures, two drops of epoxy adhesive are placed near the tips of both wires. The alignment is corrected, ensuring both tips are in contact, and more epoxy is added if needed, spreading it as close as possible to the tips, preventing any flow underneath it, and allowing them to cure like that. The substrate is then relaxed, and the two tips are squeezed together to form a larger contact. During this process, Au wets Ni as is reported on ref. [29]. To test if the sample preparation was successful, we tested its continuity with a multimeter to verify whether the contact between both electrodes was achieved.

Chapter 4

Results

4.1 Spin-Charge Transport in 3T Geometry

As seen in previous sections, in a 2T geometry circuit where a chiral component is connected in series to a ferromagnet with a node in between, the emergence of an MR signal to detect CISS is forbidden in the linear response regime according to Onsager reciprocity relations, due to chirality being invariant under time-reversal [22, 23, 21]. The only way to measure 2T MR is to break Onsager reciprocity in the nonlinear regime by introducing energy-dependent transport and energy relaxation in the device [22] or by the Hanle effect, which does not require a ferromagnetic element.

In the node, spin accumulation μ_s and electrochemical potential μ are defined, and spin is preserved. At the same time, energy relaxation takes place because of electron-phonon interaction. With this in mind, we propose to turn our heads to a 3T geometry (Fig. 4.1) following the work in ref. [32]. Here, a nonmagnetic metallic layer is in contact with the ferromagnet, playing the node's role in the previous model. This addition is experimentally justified since, in CISS experiments, the molecule needs to be attached to an affine metal, which can be done using gold with a thiol group attached to the molecule's ends [33]. The purpose of this third terminal is to measure the actual contribution of the

node (now the metallic layer). We impose the condition that this third terminal is a voltage probe; thus, the net current flowing into and out of it is zero. We aim to measure the potential difference between this new probe μ_p and μ_L .

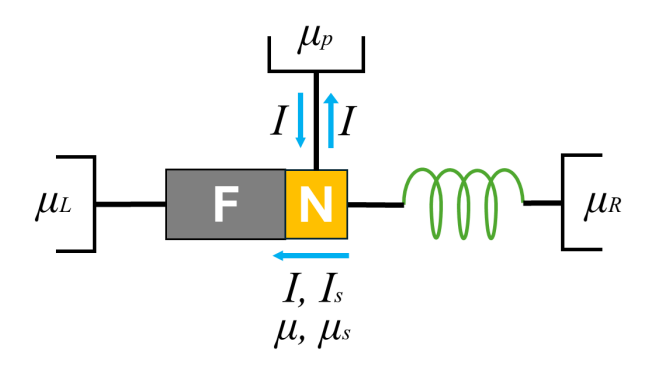


Figure 4.1: Proposed 3T circuit geometry. A third terminal has been added to the former node, which is now considered a metal layer in contact with the ferromagnet. This terminal is a measurement lead; thus, the current that flows into it has to flow out of it, causing a zero net current.

To allow easier handling, we rewrite the equations that were obtained in Yang Xu and Van Wees model, (2.94), (2.95) and (2.96):

$$\mu_s = \Gamma_2(\mu_R - \mu_L),\tag{2.94}$$

$$\mu = \mu_L - \Gamma_3(\mu_R - \mu_L), \tag{2.95}$$

$$= \mu_R + \Gamma_1(\mu_R - \mu_L). \tag{2.96}$$

The introduced variables Γ_1 , Γ_2 , and Γ_3 are defined as,

$$\Gamma_1 = \frac{-G_3^2 - G_3 g_3) - G_1 (G_4 + g_4)}{f},\tag{4.1}$$

$$\Gamma_3 = \frac{g_3^2 + G_3 g_3 - g_1 (G_4 + g_4)}{f},\tag{4.2}$$

$$\Gamma_2 = \frac{G_3 g_1 + G_1 g_3}{f}. (4.3)$$

It is now possible to consider the contribution of the spin accumulation with respect to the electrochemical potential μ_s at the far left of the ferromagnet, μ_L . Starting from the interaction of the two induced electrochemical potentials at the node, $\mu - \mu_s$ from (2.94) and (2.96),

$$\mu - \mu_s = \mu_R + \Gamma_1(\mu_L - \mu_R) - \Gamma_2(\mu_L - \mu_R), \tag{4.4}$$

we then replace the expression (2.95) for μ referred to μ_L ,

$$\mu_L - \Gamma_3(\mu_L - \mu_R) - \mu_s = \mu_R + \Gamma_1(\mu_L - \mu_R) - \Gamma_2(\mu_L - \mu_R), \tag{4.5}$$

$$\mu_L - \mu_s = \mu_R + (\Gamma_1 - \Gamma_2 + \Gamma_3)(\mu_L - \mu_R).$$
 (4.6)

We then obtain the expression for the potential difference between the left reservoir μ_L and the electric manifestation of the preference of one spin species against the other due to CISS in the molecule, that is, the spin accumulation μ_s ,

$$\mu_L - \mu_s = \mu_R + \frac{g_3^2 - G_1 g_3 - G_3 g_1 - G_3^2 - (G_1 + g_1)(G_4 + g_4)}{f}.$$
 (4.7)

Thus, the electrochemical potential difference $\mu_L - \mu_s$ does indeed depend on the reversal of both magnetization of the ferromagnet or chirality of the molecule since it depends on G_3 and g_3 , respectively. This allows us to measure the effect of CISS even in the linear response regime, breaking Onsager reciprocity that is only concerned with the 2T geometry.

4.1.1 Application of the Transport Matrix Model

Spin Valve: GMR and TMR

The validity of Yang Xu's model [22, 23], we tackled the classic spin valve for the giant magnetoresistance (GMR) and tunneling magnetoresistance (TMR) schemes. For this, we put two ferromagnetic conductors in series.

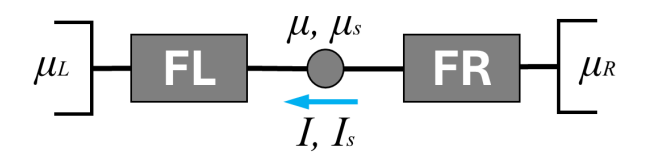


Figure 4.2: Spin valve 2T geometry circuit with two ferromagnets F1 and F2 in series. Considerations about current sign and voltage bias are the same.

The matrix equations for FR and FL, respectively, are given by:

$$\begin{pmatrix} I \\ I_s \end{pmatrix} = -\frac{\widetilde{N}}{h} \begin{pmatrix} \widetilde{T} & -\widetilde{P}_F \widetilde{T} \\ \widetilde{P}_F \widetilde{T} & -\widetilde{T} \end{pmatrix} \begin{pmatrix} \mu - \mu_R \\ \mu_s \end{pmatrix}, \tag{4.8}$$

$$= -\frac{1}{e} \begin{pmatrix} \widetilde{G}_1 & \widetilde{G}_2 \\ \widetilde{G}_3 & \widetilde{G}_4 \end{pmatrix} \begin{pmatrix} \mu - \mu_R \\ \mu_s \end{pmatrix}, \tag{4.9}$$

$$\begin{pmatrix} I \\ I_s \end{pmatrix} = -\frac{Ne}{h} \begin{pmatrix} T & -P_F T \\ P_F T & -T \end{pmatrix} \begin{pmatrix} \mu_L - \mu \\ \mu_s \end{pmatrix}, \tag{4.10}$$

$$= -\frac{1}{e} \begin{pmatrix} G_1 & G_2 \\ G_3 & G_4 \end{pmatrix} \begin{pmatrix} \mu_L - \mu \\ \mu_s \end{pmatrix}, \tag{4.11}$$

where the polarizations \widetilde{P}_F and P_F depend on the spin-specific conductances of each ferromagnet:

$$\widetilde{P}_F = \frac{\widetilde{G}_{\hookrightarrow} - \widetilde{G}_{\hookleftarrow}}{\widetilde{G}_{\hookrightarrow} + \widetilde{G}_{\hookleftarrow}},\tag{4.12}$$

$$P_F = \frac{G_{\rightarrow} - G_{\leftarrow}}{G_{\rightarrow} + G_{\leftarrow}}. (4.13)$$

Both matrix equations follow Onsager reciprocity by being antisymmetric under timereversal, as previously seen. Following the same procedure as before and considering that $G_2 = -G_3$ and $\tilde{G}_2 = -\tilde{G}_3$, we arrive at the equations for μ , μ_s , and I,

$$\mu = \mu_L - \frac{-\widetilde{G}_3^2 + G_3\widetilde{G}_3 - \widetilde{G}_1(G_4 + \widetilde{G}_4)}{f}(\mu_R - \mu_L)$$

$$= \mu_R + \frac{-G_3^2 + G_3\widetilde{G}_3 - G_1(G_4 + \widetilde{G}_4)}{f}(\mu_R - \mu_L),$$
(4.14)

$$\mu_s = \frac{G_3 \tilde{G}_1 + G_1 \tilde{G}_3}{f} (\mu_R - \mu_L), \tag{4.15}$$

$$I = -\frac{1}{e} \frac{-G_1 \widetilde{G}_3^2 - \widetilde{G}_1 G_3^2 - G_1 \widetilde{G}_1 (G_4 + \widetilde{G}_4)}{f} (\mu_R - \mu_L), \tag{4.16}$$

with f being,

$$f = -G_3^2 - \widetilde{G}_3^2 + 2G_3\widetilde{G}_3 - (G_1 + \widetilde{G}_1)(G_4 + \widetilde{G}_4). \tag{4.17}$$

Note that the current (4.16) changes depending on whether the magnetization of FL and FR are parallel or anti-parallel, since G_3 and \widetilde{G}_3 depend on P_F and \widetilde{P}_F respectively, thus changing the value of f. If the magnetizations are parallel, the product $G_3\widetilde{G}_3$ is positive, while when they are anti-parallel, it is negative. The denominator is larger in the latter case than in the former, thus making the conductance smaller in the anti-parallel and larger in the parallel configurations:

$$G_{GMR} = \frac{G_1 \tilde{G}_3^2 + \tilde{G}_1 G_3^2 + G_1 \tilde{G}_1 (G_4 + \tilde{G}_4)}{G_3^2 + \tilde{G}_3^2 - 2G_3 \tilde{G}_3 + (G_1 + \tilde{G}_1)(G_4 + \tilde{G}_4)}.$$
(4.18)

Thus, we have that,

$$G_{GMR} = G_{GMR}(P_F, \widetilde{P}_F), \tag{4.19}$$

meaning that conductance depends on the magnetization directions, and thus, we have MR signals in the linear regime. Thus, we recover the classical spin-valve GMR scheme.

To connect with the popular Julliere's model for GMR, we can see these results in terms of the density of states (DOS). From Drude's model, we know that,

$$\sigma = \frac{ne^2\tau}{m},\tag{4.20}$$

where n is the electron density, τ is the mean free time, and m is the electron mass. Electron density depends on the DOS,

$$n = \int_0^{\varepsilon_F} d\varepsilon g(\varepsilon) f(\varepsilon). \tag{4.21}$$

where $g(\varepsilon)$ is the DOS and $f(\varepsilon)$ is the Fermi-Dirac distribution. For low temperatures $f(\varepsilon) \approx \Theta(\varepsilon_F - \mu_i)$, and (4.21) becomes $n \approx g(\varepsilon_F)\varepsilon_F$. The conductance is related to the conductivity by,

$$G = \sigma \frac{A}{L} = g(\varepsilon_F)\varepsilon_F \frac{Ae^2\tau}{mL}.$$
 (4.22)

The spin-specific conductances are then,

$$G_{\uparrow} = g_{\uparrow}(\varepsilon_F)\varepsilon_F \frac{Ae^2\tau}{mL}, \quad G_{\downarrow} = g_{\downarrow}(\varepsilon_F)\varepsilon_F \frac{Ae^2\tau}{mL}.$$
 (4.23)

For each ferromagnet, we know that its spin polarization is defined in terms of its spin-specific conductance as $P_F = (G_{\uparrow} - G_{\downarrow})/(G_{\uparrow} + G_{\downarrow})$. From this and considering the spin-specific conductances, we obtain the spin polarization of each ferromagnet,

$$P_{gi} = \frac{g_{\uparrow i}(\varepsilon_F) - g_{\downarrow i}(\varepsilon_F)}{g_{\uparrow i}(\varepsilon_F) + g_{\downarrow i}(\varepsilon_F)},\tag{4.24}$$

where i = FL, FR.

The expression for the magnitude of the tunneling magnetoresistance from Julliere's model is [24],

$$GMR = \frac{R_{AP} - R_P}{R_P} = \frac{G_P - G_{AP}}{G_{AP}}$$
 (4.25)

where P means parallel and AP anti-parallel. Considering that both ferromagnets are equal, we define these resistances as,

$$R_P = \frac{2R_{\uparrow}R_{\downarrow}}{R_{\uparrow}R_{\downarrow}}, \quad G_P = \frac{1}{2}(G_{\uparrow} + G_{\downarrow}), \tag{4.26}$$

$$R_{AP} = \frac{1}{2}(R_{\uparrow} + R_{\downarrow}), \quad G_{AP} = \frac{2G_{\uparrow}G_{\downarrow}}{G_{\uparrow} + G_{\downarrow}}$$

$$(4.27)$$

Thus, we can find an expression for the GMR ratio,

$$GMR = \frac{(G_{\uparrow} - G_{\downarrow})^2}{4G_{\uparrow}G_{\downarrow}}.$$
(4.28)

If we define $\alpha = G_{\uparrow}/G_{\downarrow}$, then we can rewrite the ratio as

$$GMR = \frac{(\alpha - 1)^2}{4\alpha},\tag{4.29}$$

hence the GMR changes with the value of α , if both spin dependent conductances are equal, then GMR = 0, that is expected since it means that there's no spin preference, thus no spin valve behavior.

TMR is similar to GMR but with an insulating layer between FL and FR, thus forming a tunnel junction. The tunnel current is obtained from Fermi's golden rule on the tunneling rate [24] and considering a low bias regime, this gives

$$G_{\sigma} \approx \frac{4\pi^2 e^2}{h} T g_{\sigma L}(\varepsilon_F) g_{\sigma R}(\varepsilon_F),$$
 (4.30)

where σ is the spin direction, and T is the tunneling transmission assumed to be constant. With this in mind, the expressions for the P and AP conductances are given by [24]

$$G_P = G_P^{\uparrow} + G_P^{\downarrow} \propto (g_{\uparrow L} g_{\uparrow R} + g_{\downarrow L} g_{\downarrow R}), \tag{4.31}$$

$$G_{AP} = G_{AP}^{\uparrow} + G_{AP}^{\downarrow} \propto (g_{\uparrow L} g_{\downarrow R} + g_{\downarrow L} g_{\uparrow R}). \tag{4.32}$$

Replacing this on the TMR ratio gives,

$$TMR = \frac{R_{AP} - R_P}{R_P} = \frac{G_P - G_{AP}}{G_{AP}} \approx \frac{2P_{gFL}P_{gFR}}{1 - P_{gFL}P_{gFR}}.$$
 (4.33)

Note that if both $P_{gFL} = P_{gFR} = 1$, that is, if both ferromagnets are 100% spin-polarized, TMR becomes infinite; while if one or both ferromagnets is not polarized (i.e., $P_{gi} = 0$), then the TMR vanishes.

time-reversal Asymmetry in the Chiral Component

In Chapter 2.3, we saw that the transport matrix of the chiral component satisfied Onsager reciprocity by being symmetric (equal off-diagonal terms). This was because the chiral component had time-reversal symmetry. It is possible to break this symmetry by considering a small perturbation with odd time dependence in the transport matrix. Introducing

this component is analogous to connecting the system to a third probe that emulates dephasing processes such as electron-electron interaction, electron-phonon interaction, or inelastic impurity scattering.

Therefore, the transport matrix is:

$$\begin{pmatrix} I \\ -I_s \end{pmatrix} = -\frac{Ne}{h} \begin{pmatrix} t & (P_t - \varepsilon P_D)t \\ (P_t + \varepsilon P_D)t & \gamma_r \end{pmatrix} \begin{pmatrix} \mu_L - \mu_R \\ \mu_s \end{pmatrix}, \tag{4.34}$$

where $\varepsilon \ll 1$ is a small parameter and P_D is a contribution to the chiral component spin polarization with time-reversal asymmetry. This modified matrix satisfied Onsager reciprocity in the linear regime by being antisymmetric:

$$\mathcal{T}_{1,2}(H,M) = (P_t - \varepsilon P_D)t = T_{2,1}(-H, -M) = (P_t - \varepsilon P_D)t.$$
 (4.35)

We can proceed as normal and write the conductance equations. For this, we define the new terms in the chiral matrix:

$$\widetilde{g}_2 = \frac{Ne^2}{h}(P_t - \varepsilon P_D)t = g_2 + \varepsilon G_2^D, \tag{4.36}$$

$$\widetilde{g}_3 = \frac{Ne^2}{h}(P_t + \varepsilon P_D)t = g_3 + \varepsilon G_3^D, \tag{4.37}$$

where the superscript D stands for decoherence. Note that as before, $g_2 = g_3$ and similarly to the ferromagnet matrix elements, the decoherence terms are such that $G_2^D = -G_3^D$, defined as

$$G_2^D = -\frac{Ne^2}{h}P_D t = -G_3^D. (4.38)$$

Hence, the conductance matrices at the right and left of the node are,

$$\begin{pmatrix} I \\ -I_s \end{pmatrix} = -\frac{1}{e} \begin{pmatrix} g_1 & \widetilde{g}_2 \\ \widetilde{g}_3 & g_4 \end{pmatrix} \begin{pmatrix} \mu - \mu_R \\ \mu_s \end{pmatrix}, \tag{4.39}$$

$$\begin{pmatrix} I \\ -I_s \end{pmatrix} = -\frac{1}{e} \begin{pmatrix} G_1 & G_2 \\ G_3 & G_4 \end{pmatrix} \begin{pmatrix} \mu_L - \mu \\ \mu_s \end{pmatrix}. \tag{4.40}$$

From this, we obtain the equations for I, μ , and μ_s , which have the same form as equations (2.94)-(2.98) but with the newly defined conductances \tilde{g}_2 and \tilde{g}_3 . Considering (4.36) and (4.37), and neglecting terms with ε^2 , we obtain,

$$\mu_s = \frac{G_3 g_1 + G_1 (g_3 - \varepsilon G_3^D)}{f} (\mu_R - \mu_L), \tag{4.41}$$

$$\mu = \mu_L - \frac{g_3^2 - G_3 g_3 - \varepsilon G_3 G_3^D - G_1 (G_4 + g_4)}{f} (\mu_r - \mu_R), \tag{4.42}$$

$$= \mu_R + \frac{-G_3^2 - G_3 g_3 + \varepsilon G_3 G_3^D - G_1 (G_4 + g_4)}{f} (\mu_R - \mu_L), \tag{4.43}$$

$$I = -\frac{1}{e} \frac{G_1 g_3^2 - g_1 G_3^2 - g_1 (G_4 + g_4)}{f} (\mu_R - \mu_L), \tag{4.44}$$

$$f = g_3^2 - G_3^2 + 2\varepsilon G_3 G_3^D - (G_1 + g_1)(G_4 + g_4).$$
(4.45)

Note that now, because of the term $2\varepsilon G_3G_3^D$ in f, we have that,

$$G_{2T}^{D} = G_{2T}^{D}(P_F, P_D) = \frac{G_1 g_3^2 - g_1 G_3^2 - g_1 (G_4 + g_4)}{g_3^2 - G_3^2 + 2\varepsilon G_3 G_3^D - (G_1 + g_1)(G_4 + g_4)},$$
(4.46)

thus, it changes upon time-reversal because of the decoherence P_D term in G_3^D , and 2T MR is detectable. If we let $\varepsilon \to 0$, we recover the results in chapter 2.3. Since $\varepsilon \ll 1$, we can expand (4.46) around $\varepsilon = 0$ to first order obtaining

$$G_{2T}^{D} \approx G_{2T} + \varepsilon \frac{2G_3[G_1g_3^2 - g_1G_3^2 - G_1g_1(G_4 + g_4)]G_3^D}{[g_3^2 - G_3^2 - (G_1 + g_1)(G_4 + g_4)]^2} + \mathcal{O}(\varepsilon^2), \tag{4.47}$$

evidencing the change in the (charge) current slope. When we let $\varepsilon \to 0$, G_{2T}^D has the same expression as the usual 2T conductance restricted by reciprocity. To illustrate, a current plot is shown in Fig. 4.3 using the parameters mentioned in the plots of ref. [22], and a large ε was used to evidence the difference in both slopes for a reversal in the ferromagnet's magnetization direction. It is clear that in the vicinity of zero bias voltage (linear response), an MR signal can be measured.

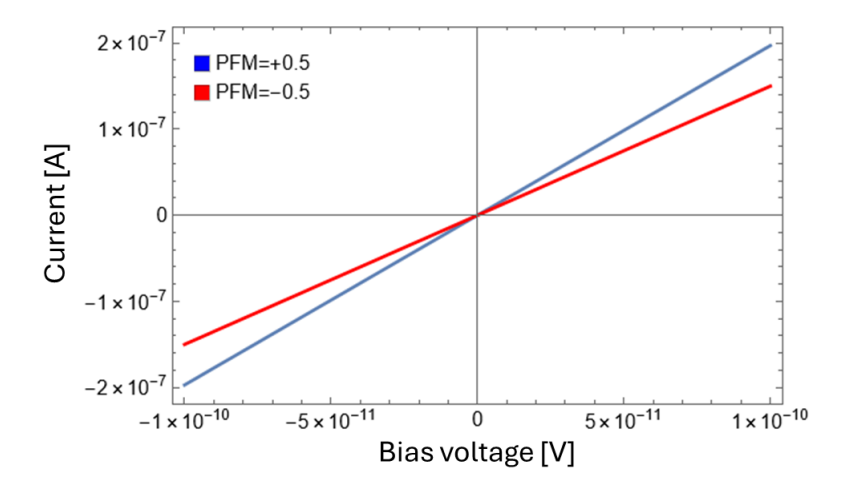


Figure 4.3: Example I-V curves due to the introduction of time-reversal symmetry breaking in the molecule's transport matrix.

4.2 Homometallic Junction

The voltage was measured under ambient conditions as a function of time as the junction elongates until it breaks. To convert the voltage traces to conductance ones, we use circuit analysis on the MCBJ. We consider that there's only one Au atom in the contact; therefore, across the junction, the current encounters a resistance of $R_{G_0} = 1/G_0 \approx 12.9k\Omega$:

$$V_{\text{out}} = V_{\text{bias}} R_f \left(\frac{1}{R_{G_0}}\right), \tag{4.48}$$

where in out case $R_f = 100 \text{ k}\Omega$ and $V_{\text{bias}} = 200 \text{ mV}$, thus $V_{\text{out}} \approx 1,54955 \text{ V}$. Dividing the output voltage of the traces by V_{out} gives us the conductance traces.

Figure 4.4a shows an individual trace of conductance measured during contact rupture. Each trace has 500 conductance measurements with a time between each measurement of $\Delta t = 2\mu$ s. The curve shows the expected step-wise decrease of the conductance, with plateaus formed around $1G_0$, $2G_0$, and $3G_0$. Not all traces were considered in the data acquisition, only those representing a whole rupture, meaning that the signal reached the minimum output voltage. The trace also shows an unexpected plateau at $1.5G_0$, possibly coming from the intrusion of contaminants in the junction.

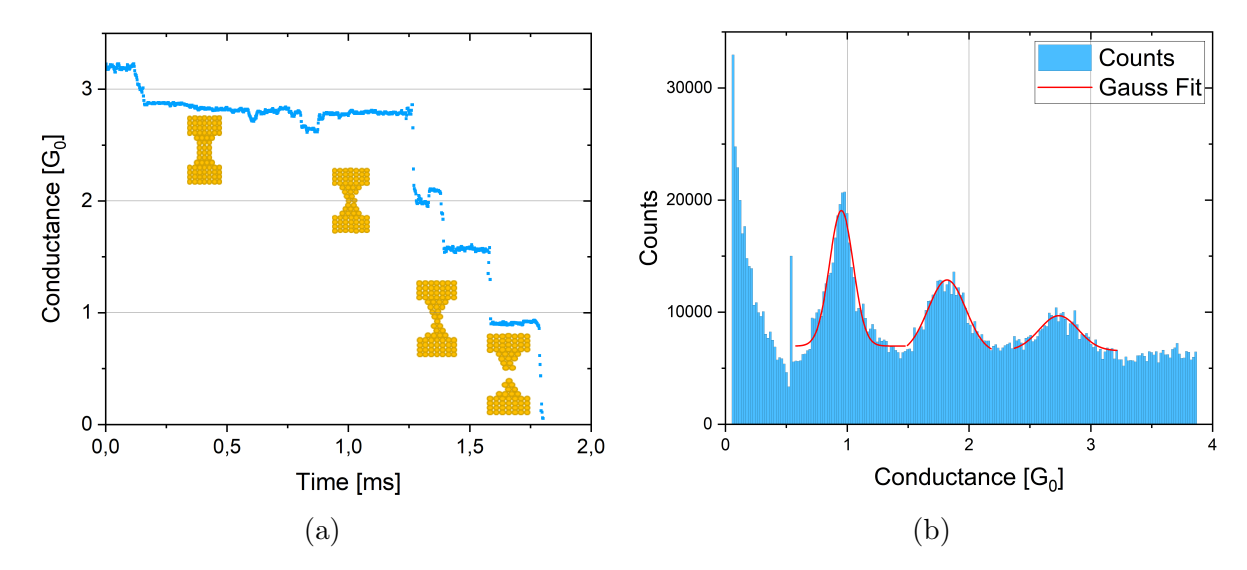


Figure 4.4: Results of the measurements taken on the Au-Au junction.(a) Individual conductance trace of a contact rupture obtained with the MCBJ device at ambient conditions with a bias voltage of 200 mV. (b) Histogram built from 5202 accumulated measurements of conductance traces during contact rupture. Three main peaks can be identified clearly, with their mean value obtained from the Gaussian fit.

Figure 4.4b shows the histogram built from 5202 accumulated conductance traces. The three main peaks are clearly visible with mean positions at $0.952 \pm 0.004 G_0$, $1.819 \pm 0.005 G_0$, and $2.737 \pm 0.01 G_0$ obtained from a Gaussian fit. The shift in the peak values is because of the different geometries the contact can assume for more than one atom in forming the contact.

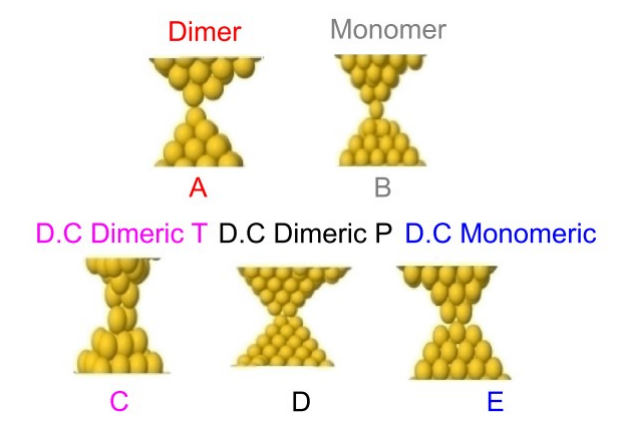


Figure 4.5: Configurations obtained from MD simulations right before first contact or just after breaking: (A) dimer, (B) monomer, (C) double contact dimeric transversal, (D) double contact dimeric parallel, and (E) double contact monomeric. From ref. [34].

In the work of Sabater et al., [34], they studied jump-to-contact (JC) and jump-out-of-contact (JOC) phenomena in gold electrodes using molecular dynamics (MD) at a constant

temperature of 4.2 K. They found that the junction takes five principal structures at the point of contact or just before breaking: dimer, monomer, double-contact dimeric transversal, double-contact dimeric parallel, and double-contact monomeric. Dimer and monomer have mean values of $0.92 \pm 0.07G_0$ and $0.97 \pm 0.15G_0$ respectively, while for all the double contact configurations, the mean value is $1.73 \pm 0.02G_0$. These structures are depicted in Fig. 4.5. Our mean conductance values are clearly well within the range of the DFT/MD results, considering that thermal effects and contaminants are present due to ambient conditions.

The histogram also shows increased counts in valleys between peaks. This is a consequence of contamination in the junction due to the lack of a controlled atmosphere. The broadening of the peaks compared to those presented in literature [28] is due to thermal effects since most of those measurements were taken under cryogenic temperatures. At $0.5G_0$, many counts were registered and appeared in other measurements taken. Further investigation is needed to find the real cause of the increased counts there, but due its sharpness we conclude that the most probable cause might be a faulty connection in the electronics or a problem with the DAQ device.

4.3 Preliminary Bimetallic Junction Results

To study bimetallic samples at room temperature, three different measurements were done: a Au-Au sample made with the bimetallic junction sample preparation technique, that is, two separate pieces of gold wire were aligned, a Ni-Ni sample made with the homometallic junction sample preparation technique, and a Au-Ni sample. All measurements were done with a 200 mV voltage bias and a 10^5 amplification factor ($R_f = 100 \text{ k}\Omega$). The obtained conductance histograms built from accumulated rupture traces are shown in Fig. 4.6.

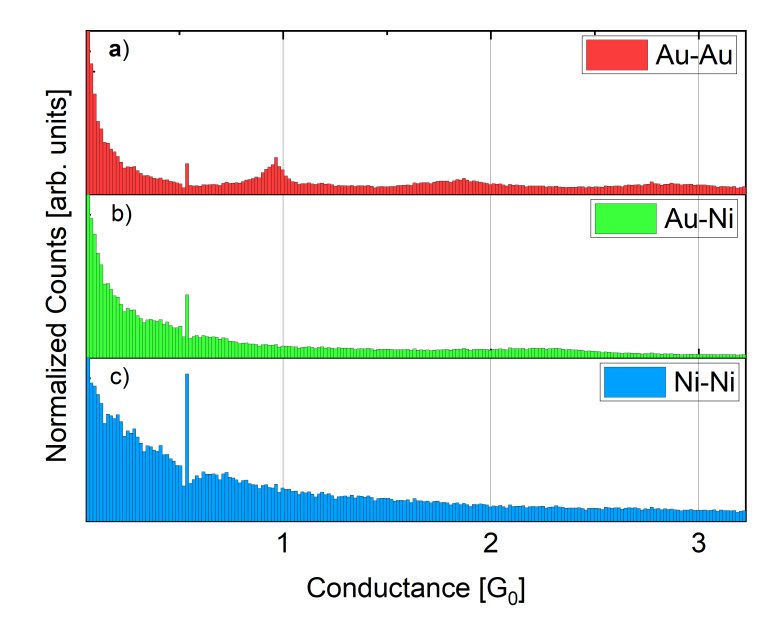


Figure 4.6: Rupture conductance histograms of homometallic and bimetallic atomic-sized junctions. (a) Conductance histogram of a homometallic Au-Au junction prepared with the bimetallic technique aligning two separate gold electrodes. (b) Conductance histogram of a bimetallic Au-Ni junction. (c) Conductance histogram of a homometallic Ni-Ni junction.

For the Au-Au sample, 5516 individual rupture traces were taken. The resulting histogram displays the three expected peaks around the first three multiple integers of the conductance quantum, but they are less pronounced than those obtained in the previous section. This might suggest that the bimetallic sample preparation technique results in weaker contact than the homometallic one. The Ni-Ni conductance histogram was built from 3072 individual rupture traces taken. Results showed only a decrease in conductance as the separation between the electrodes increased (with time). No quantization of the conductance was observed, which was expected since works done on Ni nanocontacts show that no such quantization occurs in ferromagnetic atomic-sized contacts due to the combination of the d orbitals providing several partially open conduction channels [35, 36]. But, these works describe a peak around $1.3G_0$ that is not displayed in our histogram. This vanishing might be due to oxidation of the junction since the peak was observed for theoretical calculations at cryogenic temperatures.

In the case of the Au-Ni sample, the conductance histogram was built from 3310 individual rupture traces. As previously mentioned, Tal's group showed that Au wets the

tip of the Ni electrode, forming essentially an Au-Au junction [29]. Our results did not show this behavior. Instead, it had more in common with the homometallic Ni junction, depicting only a decrease in conductance as the electrode separation increases. It's worth noting that the results obtained in ref. [29] were with the sample inside a vacuum chamber and with a temperature of 4.2 K. Meanwhile, our measurements were done in ambient conditions, meaning that oxide was formed in the tip of the nickel electrode, changing the electrical properties of the junction.

Chapter 5

Conclusions

From the work of Yang et al. [22], we saw that a two-terminal (2T) magnetoresistance (MR) measurement to determine CISS is forbidden by Onsager reciprocity relations in the linear regime. An MR signal is only measurable when we are outside the linear regime [22]. We proposed the 3T alternative, placing a third terminal connected to the node, where the spin accumulation is defined, imposing the condition that this terminal is a voltage probe. This geometry breaks Onsager reciprocity since it is only concerned with 2T but allows detecting CISS in the linear regime by measuring the potential difference between the node (a nonmagnetic metal to which the chiral molecule is coupled) and the ferromagnet. This configuration follows the idea of an emf emerging from an F/N junction with the spin being pumped from N, described in Section 2.1.2 and Ref. [24]. In the work done on CISS in photosystem I [14], a similar electric detection of CISS was used.

Another mechanism involving 2T measurement that circumvents Onsager's reciprocity is the introduction of time-reversal symmetry breaking. We modeled this in our Transport matrix approach as a small antisymmetric term in the matrix that describes the chiral molecule. With this model, we showed that spin filtering is detected in the 2T set-up in the linear regime. Time-reversal symmetry breaking can be modeled explicitly through the coefficients of the transport matrix using Green's function formalism.

On the experimental side, we have built a reliable, robust, and complete MCBJ setup capable of studying electron transport through atomic-sized contacts in homometallic, bimetallic, and possibly molecular junctions. The results obtained for the Au-Au junction showed well-defined peaks in the built histogram, comparable to those under the same conditions and at cryogenic temperatures in the literature for both the MCBJ and STM-BJ devices [30, 28].

To implement the measurement of spin-sensitive magnetoresistance, we found in the recent literature [29] the possibility of generating metal-oxide-ferro junctions using bimetal-lic contacts in the break junction set-up. This will be possible by registering the I-V curve, depending on the ferro orientation. Further refinements of our set-up are necessary to achieve this goal.

We performed the first trials of bimetallic contacts with Au-Ni junctions. We first measured homometallic gold junctions prepared as a bimetallic sample by aligning the tips of the two electrodes. The results validated the method by showing the expected conductance histogram depicting peaks around the integer multiples of the conductance quantum. We then tested homometallic nickel junctions, obtaining a conductance histogram different from the literature that depicts a decrease in the measured conductance as the contact breaks. A similar behavior was observed in the conductance histogram of the bimetallic Au-Ni junction, disagreeing with the observed wetting of the nickel tip at 4.2 K, forming suspended Au chains in the junction that gave rise to a conductance histogram similar to that of homometallic gold samples. Thus, we confirm that we must implement an atmosphere and temperature control in our set-up to carry out measurements in bimetallic samples.

Carrying out the measurements at ambient conditions implies the inevitable intrusion of contaminants in the junction that, combined with thermal effects, account for the broadening of the peaks and the increased counts in the valleys of the conductance histogram of the homometallic sample. A higher number of measurements is needed so that these effects pale against the actual conductance values being measured. Since we opted

to utilize PLA 3D-printed strips as our flexible substrates, many repeated measurements could lead to permanent deformation; a more flexible material like phosphorous bronze might be the best option. Contamination is a bigger deal for the bimetallic samples because we must keep the substrate bent and the sample exposed for at least twenty-four hours to allow the epoxy drops to cure. Therefore, contaminants and oxide accumulate in the junction in the case of Ni samples. This also means that a high-quality flexible substrate is a must.

5.1 Future Work

Building on the foundation of this work, we aim to investigate CISS with the MCBJ set-up to study transport through molecular contacts using oligopeptides. This involves using a bimetallic junction (Au-Ni) and placing the oligopeptides between both electrodes. We are currently adapting our set-up to operate inside a vacuum chamber, allowing measurements under low vacuum and in an inert argon atmosphere, controlling the environment and preventing contamination. We are building a vibration isolation system to enhance measurement stability, allowing the study of transport through chains of atoms or single molecules without breaking the contact due to their vibration sensitivity.

We must develop a molecule deposition technique to place the oligopeptides between the two electrodes. After a brief but insightful discussion with Prof. Oren Tal of the Department of Chemical and Biological Physics, Weizmann Institute of Science, we have decided to develop a molecule atomizer like the one they designed in ref. [37]. It heats a drop of the oligopeptide solution and evaporates it, directing the flush of molecules toward the junction through a small nozzle. They have also enlightened that to remove the oxide formed on the junction, high voltage pulses should be applied to inject current from the Ni to the Au, and manual squeezing should be done to encourage Ni wetting by Au. With these additions to our set-up, we plan to measure conductance through a single oligopeptide and characterize I-V under different magnetization directions of the nickel electrode to explore the spin-selective transport associated with CISS.

Bibliography

- [1] Bernd Giese. Electron transfer in dna. Current Opinion in Chemical Biology, 6(5):612–618, 2002.
- [2] Stuart Lindsay. Ubiquitous electron transport in non-electron transfer proteins. *Life*, 10(5), 2020.
- [3] P S Farago. Spin-dependent features of electron scattering from optically active molecules. *Journal of Physics B: Atomic and Molecular Physics*, 13(18):L567, sep 1980.
- [4] P S Farago. Electron optic dichroism and electron optic activity. *Journal of Physics B: Atomic and Molecular Physics*, 14(22):L743, nov 1981.
- [5] S Mayer, C Nolting, and J Kessler. Electron scattering from chiral molecules. *Journal of Physics B: Atomic, Molecular and Optical Physics*, 29(15):3497, aug 1996.
- [6] K Blum and D Thompson. Spin-dependent electron scattering from oriented molecules. Journal of Physics B: Atomic, Molecular and Optical Physics, 22(11):1823, 1989.
- [7] C Johnston, K Blum, and D Thompson. Chiral effects in spin-dependent elastic electron scattering from molecules. *Journal of Physics B: Atomic, Molecular and Optical Physics*, 26(5):965, 1993.

- [8] K. Ray, S. P. Ananthavel, D. H. Waldeck, and R. Naaman. Asymmetric scattering of polarized electrons by organized organic films of chiral molecules. *Science*, 283(5403):814–816, 1999.
- [9] B. Göhler, V. Hamelbeck, T. Z. Markus, M. Kettner, G. F. Hanne, Z. Vager, R. Naaman, and H. Zacharias. Spin selectivity in electron transmission through self-assembled monolayers of double-stranded dna. *Science*, 331(6019):894–897, 2011.
- [10] Zouti Xie, Tal Z. Markus, Sidney R. Cohen, Zeev Vager, Rafael Gutierrez, and Ron Naaman. Spin specific electron conduction through dna oligomers. Nano Letters, 11(11):4652–4655, 2011. PMID: 21961931.
- [11] Albert C Aragonès, Ernesto Medina, Miriam Ferrer-Huerta, Nuria Gimeno, Meritxell Teixidó, Julio L Palma, Nongjian Tao, Jesus M Ugalde, Ernest Giralt, Ismael Díez-Pérez, et al. Measuring the spin-polarization power of a single chiral molecule. small, (2):1602519, 2017.
- [12] M Kettner, B Gohler, H Zacharias, D Mishra, V Kiran, R Naaman, Claudio Fontanesi, David H Waldeck, Slawomir Sek, Jan Pawlowski, et al. Spin filtering in electron transport through chiral oligopeptides. The Journal of Physical Chemistry C, 119(26):14542–14547, 2015.
- [13] DH Waldeck, R Naaman, and Y Paltiel. The spin selectivity effect in chiral materials.

 APL materials, 9(4), 2021.
- [14] Itai Carmeli, Karuppannan Senthil Kumar, Omri Heifler, Chanoch Carmeli, and Ron Naaman. Spin selectivity in electron transfer in photosystem i. Angewandte Chemie International Edition, 53(34):8953–8958, 2014.
- [15] Mohammad Reza Safari, Frank Matthes, Claus M. Schneider, Karl-Heinz Ernst, and Daniel E. Bürgler. Spin-selective electron transport through single chiral molecules. Small, 20(22), December 2023.
- [16] Ana M. Ortuño, Pablo Reiné, Luis Álvarez de Cienfuegos, Irene R. Márquez, Wynand Dednam, Enrico B. Lombardi, Juan J. Palacios, Edmund Leary, Giovanna

- Longhi, Vladimiro Mujica, Alba Millán, M. Teresa González, Linda A. Zotti, Delia Miguel, and Juan M. Cuerva. Chiral single-molecule potentiometers based on stapled ortho-oligo(phenylene)ethynylenes. *Angewandte Chemie International Edition*, 62(16):e202218640, 2023.
- [17] Solmar Varela, Vladimiro Mujica, and Ernesto Medina. Effective spin-orbit couplings in an analytical tight-binding model of dna: Spin filtering and chiral spin transport. *Phys. Rev. B*, 93:155436, Apr 2016.
- [18] Ai-Min Guo and Qing-feng Sun. Spin-selective transport of electrons in dna double helix. *Physical review letters*, 108(21):218102, 2012.
- [19] Ai-Min Guo and Qing-Feng Sun. Spin-dependent electron transport in proteinlike single-helical molecules. Proceedings of the National Academy of Sciences, 111(32):11658–11662, 2014.
- [20] Ai-Min Guo, Ting-Rui Pan, Tie-Feng Fang, XC Xie, and Qing-Feng Sun. Spin selectivity effect in achiral molecular systems. *Physical Review B*, 94(16):165409, 2016.
- [21] Xu Yang, Caspar H. van der Wal, and Bart J. van Wees. Spin-dependent electron transmission model for chiral molecules in mesoscopic devices. *Physical Review B*, 99(2), January 2019.
- [22] Xu Yang, Caspar H. van der Wal, and Bart J. van Wees. Detecting chirality in two-terminal electronic nanodevices. *Nano Letters*, 20(8):6148–6154, 2020. PMID: 32672980.
- [23] Xu Yang. Connecting chirality and spin in electronic devices. PhD thesis, University of Groningen, 2020.
- [24] Jaroslav Fabian, Alex Matos-Abiague, Christian Ertler, Peter Stano, and Igor Žutić. Semiconductor spintronics. *Acta Physica Slovaca*, 57(4-5):565–907, August 2007.

- [25] Mark Johnson. Spin injection in metals and semiconductors. Semiconductor Science Technology, 17(4):298–309, apr 2002.
- [26] Horacio M. Pastawski and Ernesto Medina. Tight binding methods in quantum transport through molecules and small devices: From the coherent to the decoherent description. Revista Mexicana de Fisica, 47(SUPPL. 1):1–23, mar 2001.
- [27] Sytze H Tirion and Bart J van Wees. Mechanism for electrostatically generated magnetoresistance in chiral systems without spin-dependent transport. ACS nano, 18(8):6028–6037, 2024.
- [28] Nicolás Agrait, Alfredo Levy Yeyati, and Jan M. van Ruitenbeek. Quantum properties of atomic-sized conductors. *Physics Reports*, 377(2):81–279, 2003.
- [29] Anil Kumar Singh, Sudipto Chakrabarti, Ayelet Vilan, Alexander Smogunov, and Oren Tal. Electrically controlled bimetallic junctions for atomic-scale electronics. Nano Letters, 23(17):7775–7781, 2023. PMID: 37603598.
- [30] Carla Borja, Carlos Sabater, Carlos Untiedt, Ernesto Medina, and Werner Brämer-Escamilla. Conductance quantization in atomic-sized gold contacts using a low-cost mechanically controllable break junction setup. European Journal of Physics, 41(6):065401, oct 2020.
- [31] Stefan Egle, Cecile Bacca, Hans-Fridtjof Pernau, Magdalena Huefner, Denise Hinzke, Ulrich Nowak, and Elke Scheer. Magnetoresistance of atomic-size contacts realized with mechanically controllable break junctions. *Physical Review B—Condensed Matter and Materials Physics*, 81(13):134402, 2010.
- [32] Miguel Angel Sanmartin Castillo. Two terminal devices for the ciss effect analytical and modeling. B.S. thesis, Universidad de Investigación de Tecnología Experimental Yachay, 2022.
- [33] Claude Nogues, Sidney R Cohen, Shirley S Daube, and Ron Naaman. Electrical properties of short dna oligomers characterized by conducting atomic force microscopy. Physical Chemistry Chemical Physics, 6(18):4459–4466, 2004.

- [34] Carlos Sabater, María José Caturla, Juan José Palacios, and Carlos Untiedt. Understanding the structure of the first atomic contact in gold. *Nanoscale Research Letters*, 8(1), May 2013.
- [35] M. Häfner, J. K. Viljas, D. Frustaglia, F. Pauly, M. Dreher, P. Nielaba, and J. C. Cuevas. Theoretical study of the conductance of ferromagnetic atomic-sized contacts. *Phys. Rev. B*, 77:104409, Mar 2008.
- [36] F. Pauly, M. Dreher, J. K. Viljas, M. Häfner, J. C. Cuevas, and P. Nielaba. Theoretical analysis of the conductance histograms and structural properties of ag, pt, and ni nanocontacts. *Phys. Rev. B*, 74:235106, Dec 2006.
- [37] Tamar Yelin, Richard Korytár, Nirit Sukenik, Ran Vardimon, Bhupesh Kumar, C Nuckolls, Ferdinand Evers, and Oren Tal. Conductance saturation in a series of highly transmitting molecular junctions. *Nature materials*, 15(4):444–449, 2016.
- [38] R Jansen, A Spiesser, H Saito, Y Fujita, S Yamada, K Hamaya, and S Yuasa. Non-linear electrical spin conversion in a biased ferromagnetic tunnel contact. *Physical Review Applied*, 10(6):064050, 2018.

Appendix A

Transport Matrix for the Chiral Component

In this section, we will show in detail how the transport matrix for the chiral component is obtained starting from the Landauer-Buttiker formula. We start from the two spin-space transmission and reflection matrices for the right and left moving electrons introduced in the main text [22]:

$$\mathbb{T}_{\triangleright} = \begin{pmatrix} t_{\to \to} & t_{\leftarrow \to} \\ t_{\to \leftarrow} & t_{\leftarrow \leftarrow} \end{pmatrix}, \qquad \mathbb{R}_{\triangleright} = \begin{pmatrix} r_{\to \to} & r_{\leftarrow \to} \\ r_{\to \leftarrow} & r_{\leftarrow \leftarrow} \end{pmatrix}, \qquad (A.1)$$

$$\mathbb{T}_{\triangleleft} = \begin{pmatrix} t_{\leftarrow \leftarrow} & t_{\to \leftarrow} \\ t_{\leftarrow \to} & t_{\to \to} \end{pmatrix}, \qquad \mathbb{R}_{\triangleleft} = \begin{pmatrix} r_{\leftarrow \leftarrow} & r_{\to \leftarrow} \\ r_{\leftarrow \to} & r_{\to \to} \end{pmatrix}. \qquad (A.2)$$

$$\mathbb{T}_{\triangleleft} = \begin{pmatrix} t_{\leftarrow\leftarrow} & t_{\rightarrow\leftarrow} \\ t_{\leftarrow\rightarrow} & t_{\rightarrow\rightarrow} \end{pmatrix}, \qquad \mathbb{R}_{\triangleleft} = \begin{pmatrix} r_{\leftarrow\leftarrow} & r_{\rightarrow\leftarrow} \\ r_{\leftarrow\rightarrow} & r_{\rightarrow\rightarrow} \end{pmatrix}. \tag{A.2}$$

We use the Landauer-Buttiker formula from section 2.2 to find the current that leaves each lead. For the left lead, we have

$$I_{L} = e \int d\varepsilon \left[T_{R,L} v_{L} \frac{1}{2} N_{L}(\varepsilon) f_{L}(\varepsilon) - T_{L,R} v_{R} \frac{1}{2} N_{R}(\varepsilon) f_{R}(\varepsilon) \right], \tag{A.3}$$

where the DOS $N_i(\varepsilon) = 1/\pi (dk/d\varepsilon)$, and knowing that the group velocity of electrons is given by $v_i = d\omega/dk = 1/\hbar (d\varepsilon/dk)$, then we obtain that

$$N_i(\varepsilon) = \frac{1}{\pi \hbar v_i} = \frac{2}{h v_i}.$$
 (A.4)

Replacing the DOS in the current I_L , we obtain

$$I_{L} = \frac{e}{h} \int d\varepsilon \left[T_{R,L}(\varepsilon) f_{L}(\varepsilon) - T_{L,R}(\varepsilon) f_{R}(\varepsilon) \right]. \tag{A.5}$$

If we now consider that, as in section 2.2, the temperature is low and the time-reversal for the transmission probabilities such that $T_{R,L} = T_{L,R}$, then we obtain

$$I_{L} = \frac{e}{h} \left[T_{R,L} \mu_{L} - T_{L,R} \mu_{R} \right]$$
 (A.6)

Note that the first term refers to the current injected from the left lead, and the right one refers to the current coming into it. We can write the first term depending on the reflection back to the left lead as $1 - R_{L,L}$:

$$I_L = \frac{e}{h} \left[(1 - R_{L,L})\mu_L - T_{L,R}\mu_R \right]. \tag{A.7}$$

If we now consider the spin-dependence of each variable, we can write the spin-space column vector version:

$$\begin{pmatrix} I_{L\to} \\ I_{L\leftarrow} \end{pmatrix} = -\frac{Ne}{h} \left[(\mathbb{I} - \mathbb{R}_{\triangleright}) \begin{pmatrix} \mu_{L\to}, \\ \mu_{L\leftarrow} \end{pmatrix} - \mathbb{T}_{\triangleleft} \begin{pmatrix} \mu_{R\to} \\ \mu_{R\leftarrow} \end{pmatrix} \right], \tag{A.8}$$

$$\begin{pmatrix} I_{R\to} \\ I_{R\leftarrow} \end{pmatrix} = \frac{Ne}{h} \left[(\mathbb{I} - \mathbb{R}_{\triangleleft}) \begin{pmatrix} \mu_{R\to} \\ \mu_{R\leftarrow} \end{pmatrix} - \mathbb{T}_{\triangleright} \begin{pmatrix} \mu_{L\to} \\ \mu_{L\leftarrow} \end{pmatrix} \right], \tag{A.9}$$

the current on lead L is negative because we have assumed that the current moving from left to right is negative and from right to left is positive.

From (A.8) and replacing the directional transmission and reflection matrices, we obtain

$$I_{L\to} = -\frac{Ne}{h}[(1 - r_{\to\to})\mu_{L\to} - r_{\leftarrow\to}\mu_{L\leftarrow} - t_{\leftarrow\leftarrow}\mu_{R\to} - t_{\to\leftarrow}\mu_{R\leftarrow}], \tag{A.10}$$

$$I_L \leftarrow = -\frac{Ne}{h} [-r_{\to\leftarrow} \mu_{L\to} + (1 - r_{\leftarrow\leftarrow}) \mu_{L\leftarrow} - t_{\leftarrow\to} \mu_{R\to} - t_{\to\to} \mu_{R\leftarrow}]. \tag{A.11}$$

Therefore, we can now find the expressions for $I = I_{L\rightarrow} + I_{L\leftarrow}$:

$$I = -\frac{Ne}{h} [(1 - r_{\to \to} - r_{\to \leftarrow}) \mu_{L\to} + (1 - r_{\leftarrow \leftarrow} - r_{\leftarrow \to}) \mu_{L\leftarrow} - (t_{\leftarrow \leftarrow} + t_{\leftarrow \to}) \mu_{R\to} - (t_{\to \leftarrow} + t_{\to \to}) \mu_{R\leftarrow}], \tag{A.12}$$

using the fact that $\mu_{i\rightarrow} = \mu_i + \mu_{si}$ and $\mu_{i\leftarrow} = \mu_i - \mu_{si}$,

$$I = -\frac{Ne}{h} [(1 - r_{\to \to} - r_{\to \leftarrow} + 1 - r_{\leftarrow \leftarrow} - r_{\leftarrow \to})\mu_{L}$$

$$+ (1 - r_{\to \to} - r_{\to \leftarrow} - 1 + r_{\leftarrow \leftarrow} + r_{\leftarrow \to})\mu_{sL}$$

$$- (t_{\leftarrow \leftarrow} + t_{\leftarrow \to} + t_{\to \leftarrow} + t_{\to \to})\mu_{R}$$

$$+ (-t_{\leftarrow \leftarrow} - t_{\leftarrow \to} + t_{\to \leftarrow} + t_{\to \to})\mu_{sR}]$$
(A.13)

Finally, considering the definitions (2.70)-(2.77), we obtain the equation of the current across the chiral component

$$I = -\frac{Ne}{h}[(\mu_L - \mu_R)t + \mu_{sL}s + \mu_{sR}s]. \tag{A.14}$$

Due to continuity, this result should be the same as $I = I_{R \to} + I_{R \leftarrow}$.

Now we find the expression for $I_{sL} = I_{L\rightarrow} - I_{L\leftarrow}$:

$$I_{sL} = -\frac{Ne}{h} [(1 - r_{\rightarrow \rightarrow} + r_{\rightarrow \leftarrow})\mu_{L\rightarrow} + (-1 - r_{\leftarrow \leftarrow} + r_{\leftarrow \rightarrow})\mu_{L\leftarrow} + (-t_{\leftarrow \leftarrow} + t_{\leftarrow \rightarrow})\mu_{R} \rightarrow + (-t_{\rightarrow \leftarrow} + t_{\rightarrow \rightarrow})\mu_{R\leftarrow}],$$

$$= -\frac{Ne}{h} [(1 - r_{\rightarrow \rightarrow} + r_{\rightarrow \leftarrow} - 1 - r_{\leftarrow \leftarrow} + r_{\leftarrow \rightarrow})\mu_{L}$$

$$+ (1 - r_{\rightarrow \rightarrow} + r_{\rightarrow \leftarrow} + 1 + r_{\leftarrow \leftarrow} - r_{\leftarrow \rightarrow})\mu_{sL}$$

$$+ (-t_{\leftarrow \leftarrow} + t_{\leftarrow \rightarrow} - t_{\rightarrow \leftarrow} + t_{\rightarrow \rightarrow})\mu_{R}$$

$$+ (-t_{\leftarrow \leftarrow} + t_{\leftarrow \rightarrow} + t_{\rightarrow \leftarrow} - t_{\rightarrow \rightarrow})\mu_{sR}],$$

$$= -\frac{Ne}{h} [-P_{r}r\mu_{L} - \gamma_{r}\mu_{sL} + P_{t}t\mu_{R} - \gamma_{t}\mu_{sR}]. \tag{A.16}$$

In this last expression, we consider that Onsager reciprocity needs that $P_t t = P_r r = s$; thus we write

$$I_{sL} = \frac{Ne}{h} [(\mu_L - \mu_R) P_r r + \gamma_r \mu_{sL} + \gamma_t \mu_{sR}].$$
 (A.17)

Following a similar procedure for I_{sR} ,

$$I_{sR} = -\frac{Ne}{h} [(\mu_L - \mu_R) P_t t + \gamma_t \mu_{sL} + \gamma_r \mu_{sR}].$$
 (A.18)

Thus, we finally obtain the 3×3 transport matrix for the chiral component:

$$\begin{pmatrix} I \\ -I_{sL} \\ I_{sR} \end{pmatrix} = -\frac{Ne}{h} \begin{pmatrix} t & s & s \\ P_r r & \gamma_r & \gamma_t \\ P_t t & \gamma_t & \gamma_r \end{pmatrix} \begin{pmatrix} \mu_L - \mu_R \\ \mu_{sL} \\ \mu_{sR} \end{pmatrix}. \tag{A.19}$$

Appendix B

Transport Matrix for the FMTJ

In this section, we will show in detail how the transport matrix for the ferromagnetic tunnel junction (FMTJ) is obtained. We start from the tunnel currents for majority (\rightarrow) and minority (\leftarrow) spin electrons as discussed in ref.[38]:

$$I_{\to} = G_{\to} \left(V - \frac{\mu_{sR}}{e} \right), \tag{B.1}$$

$$I_{\leftarrow} = G_{\leftarrow} \left(V + \frac{\mu_{sR}}{e} \right), \tag{B.2}$$

where $V = -(\mu_L - \mu)/e$ is the voltage bias between the left lead and the node. Replacing this, we get

$$I_{\rightarrow} = -\frac{G_{\rightarrow}}{e} \left(\mu_L - \mu - \mu_{sR} \right), \tag{B.3}$$

$$I_{\leftarrow} = -\frac{G_{\leftarrow}}{e} \left(\mu_L - \mu + \mu_{sR} \right). \tag{B.4}$$

Hence, we can now find $I = I_{\rightarrow} + I_{\leftarrow}$ and $I_{sR} = I_{\rightarrow} - I_{\leftarrow}$, with the latter being at the left side of the node:

$$I = -\frac{1}{e}[G_{\to}\mu_L - G_{\to}\mu_R - G_{\to}\mu_{sR} + G_{\leftarrow}\mu_L - G_{\leftarrow}\mu_R + G_{\leftarrow}\mu_{sR}],$$
 (B.5)

$$= -\frac{1}{e}[(\mu_L - \mu_R)G_F - \mu_{sR}G_F P_F], \tag{B.6}$$

$$I_{sR} = -\frac{1}{e} [G_{\to} \mu_L - G_{\to} \mu_R - G_{\to} \mu_{sR} - G_{\leftarrow} \mu_L + G_{\leftarrow} \mu_R - G_{\leftarrow} \mu_{sR}], \tag{B.7}$$

$$= -\frac{1}{e}[(\mu_L - \mu_R)G_F P_F - \mu_{sR}G_F], \tag{B.8}$$

were we have used the definitions of the Ferromagnet spin-polarization $P_F = (G_{\rightarrow} - G_{\leftarrow})/(G_{\rightarrow} + G_{\leftarrow})$ and the total conductance $G_F = G_{\rightarrow} + G_{\leftarrow}$. To distinguish G_F from ideal transmission, a transmission coefficient T (0 $\leq T \leq$ 0) is introduced so that we decouple how well the junction conducts overall from the spin polarization effects [22]:

$$I = -\frac{N'e}{h}[(\mu_L - \mu_R)T - \mu_{sR}P_F T],$$
(B.9)

$$I_{sR} = -\frac{N'e}{h} [(\mu_L - \mu_R)P_F T - \mu_{sR} T], \tag{B.10}$$

therefore, we obtain the ferromagnet's transport matrix:

$$\begin{pmatrix} I \\ I_{sR} \end{pmatrix} = -\frac{N'e}{h} \begin{pmatrix} T & -P_F T \\ P_F T & -T \end{pmatrix} \begin{pmatrix} \mu_L - \mu_R \\ \mu_{sR} \end{pmatrix}. \tag{B.11}$$

Appendix C

2T Spin-Charge Transport

With the transport matrices for each component obtained, we can study spin and charge transport when both are connected in series in a two-terminal (2T) configuration. As in section 2.3.3, we rewrite the transport equations into conductance equations:

$$\begin{pmatrix} I \\ -I_s \end{pmatrix} = -\frac{1}{e} \begin{pmatrix} g_1 & g_2 \\ g_3 & g_4 \end{pmatrix} \begin{pmatrix} \mu - \mu_R \\ \mu_s \end{pmatrix}, \tag{C.1}$$

$$\begin{pmatrix} I \\ -I_s \end{pmatrix} = -\frac{1}{e} \begin{pmatrix} G_1 & G_2 \\ G_3 & G_4 \end{pmatrix} \begin{pmatrix} \mu_L - \mu \\ \mu_s \end{pmatrix}, \tag{C.2}$$

where the matrix elements for the chiral component are given by:

$$g_1 = \frac{Ne^2}{h}t,\tag{C.3}$$

$$g_2 = \frac{Ne^2}{h}P_t t = g_3, \tag{C.4}$$

$$g_4 = -\frac{Ne^2}{h} \left(1 + \frac{2P_t}{\eta_r} \right) t, \tag{C.5}$$

where $g_2 = g_3$ due to the matrix being symmetric because of Onsager reciprocity. Similarly, the matrix elements for the FMTJ are:

$$G_1 = \frac{N'e^2}{h}T,\tag{C.6}$$

$$G_2 = -\frac{N'e^2}{h}P_FT = -G_3,$$
 (C.7)

$$G_4 = -\frac{-N'e^2}{h}T. (C.8)$$

Here, $G_2 = -G_3$ because the matrix is antisymmetric. At the steady state, continuity requires I and I_s to be equal at both sides of the node. From C.1 and C.2, respectively, we have:

$$I = -\frac{1}{e}[G_1(\mu_L - \mu) + G_2\mu_s], \tag{C.9}$$

$$I_s = -\frac{1}{e}[G_3(\mu_L - \mu) + G_4\mu_s], \qquad (C.10)$$

$$I = -\frac{1}{e}[g_1(\mu - \mu_R) + g_2\mu_s], \tag{C.11}$$

$$-I_s = \frac{1}{e} [g_3(\mu - \mu_R) + g_4 \mu_s]. \tag{C.12}$$

Thus, equating (C.9) and (C.12):

$$\mu = \frac{G_1 \mu_L + (G_2 - g_2)\mu_s + g_1 \mu_R}{G_1 + g_1}.$$
 (C.13)

Equating (C.12) and (C.10) with the latter being multiplied by -1:

$$\mu = \frac{G_3\mu_L + (G_4 + g_4)\mu_s - g_3\mu_R}{G_3 - g_3}.$$
 (C.14)

Now, equating the two obtained equations for μ :

$$(G_3 - g_3)[G_1\mu_L + (G_2 - g_2)\mu_s + g_1\mu_R] = (G_1 + g_1)[G_3\mu_L + (G_4 + g_4)\mu_s - g_3\mu_R],$$
$$[(G_3 - g_3)(G_2 - g_2) - (G_1 + g_1)(G_4 + g_4)]\mu_s = (g_1G_3 + g_3G_1)\mu_L - (G_1g_3 + G_3g_1)\mu_R,$$

where we define the term on the left-hand side as $f = (G_3 - g_3)(G_2 - g_2) - (G_1 + g_1)(G_4 + g_4)$:

$$\mu_s = \frac{g_1 G_3 + g_3 G_1}{f} (\mu_L - \mu_R). \tag{C.15}$$

Replacing this expression for μ_s into (C.13):

$$\mu = \frac{G_1\mu_L + g_1\mu_R}{G_1 + g_1} + \frac{G_2 - g_2}{G_1 + g_1} \frac{g_1G_3 + g_3G_1}{f} (\mu_L - \mu_R),$$

$$= \frac{(G_1\mu_L + g_1\mu_R)f + (G_2 - g_2)(g_1G_3 + g_3G_1)(\mu_L - \mu_R)}{(G_1 + g_1)f},$$

$$= \frac{(G_1 + g_1)\{[G_3(G_2 - g_2) - G_1(G_4 + g_4)]\mu_L - [g_3(G_2 - g_2) - g_1(G_4 + g_4)]\mu_R\}}{(G_1 + g_1)f},$$

adding and subtracting $[-g_3(g_2 - G_2) + g_1(G_4 + g_4)]\mu_L/f$,

$$\mu = -\frac{g_3(g_2 - G_2) - g_1(G_4 + g_4)}{f}(\mu_L - \mu_R) + \frac{(G_3 - g_3)(G_2 - g_2) - (G_1 + g_1)(G_4 + g_4)}{f}\mu_L.$$

Noting that the numerator of the second term is f, then we obtain the expression for μ referred to the left lead:

$$\mu = \mu_L - \frac{g_3(g_2 - G_2) - g_1(G_4 + g_4)}{f} (\mu_L - \mu_R). \tag{C.16}$$

Replacing now the expression for μ_s on (C.14):

$$\begin{split} \mu = & \frac{G_3\mu_L - g_3\mu_R}{G_3 - g_3} + \frac{G_4 + g_4}{G_3 - g_3} \frac{g_1G_3 + g_3G_1}{f} (\mu_L - \mu_R), \\ = & \frac{(G_3\mu_L - g_3\mu_R)f + (G_4 + g_4)(g_1G_3 + g_3G_1)(\mu_L - \mu_R)}{(G_3 - g_3)f}, \\ = & \frac{(G_3 - g_3)\{[G_3(G_2 - g_2) - G_1(G_4 + g_4)]\mu_L - [g_3(G_2 - g_2) - g_1(G_4 + g_4)]\mu_R\}}{(G_3 - g_3)f}. \end{split}$$

adding and subtracting $[G_3(G_2 - g_2) - G_1(G_4 + g_4)]\mu_R/f$,

$$\mu = \frac{G_3(G_2 - g_2) - G_1(G_4 + g_4)}{f}(\mu_L - \mu_R) + \frac{G_3 - g_3}{f}(G_2 - g_2) - (G_1 + g_1)(G_4 + g_4)f\mu_R.$$

The numerator of the second term is once again equal to f; therefore, we obtain the expression for μ referred to the right lead:

$$\mu = \mu_R + \frac{G_3(G_2 - g_2) - G_1(G_4 + g_4)}{f}(\mu_L - \mu_R). \tag{C.17}$$

We still need to find I and I_s . We look back at equation (C.11) and replace the expressions for both μ and μ_s :

$$I = -\frac{1}{e} \left[G_1 \frac{g_3(g_2 - G_2) - g_1(G_4 + g_4)}{f} (\mu_L - \mu_R) + G_2 \frac{g_1 G_3 + g_3 G_1}{f} (\mu_L - \mu_R) \right],$$

= $-\frac{1}{e} \frac{G_1 g_2 g_3 - G_1 G_2 g_3 - G_1 g_1 G_4 - G_1 g_1 g_4 + g_1 G_2 G_3 + G_1 G_2 g_3}{f} (\mu_L - \mu_R),$

simplifying, we obtain the expression for the current in the system:

$$I = -\frac{1}{e} \frac{G_1 g_2 g_3 + g_1 G_2 G_3 - G_1 g_1 (G_4 + g_4)}{f} (\mu_L - \mu_R).$$
 (C.18)

Where, noting that the bias voltage is given by $V = -(\mu_L - \mu_R)/e$, thus we have the expression for the 2T conductance discussed in the main text.

Finally, we find an expression for I_s by substituting the expressions of μ and μ_s in (C.10):

$$\begin{split} I &= -\frac{1}{e} \left[G_3 \frac{g_3(g_2 - G_2) - g_1(G_4 + g_4)}{f} (\mu_L - \mu_R) + G_4 \frac{g_1 G_3 + g_3 G_1}{f} (\mu_L - \mu_R) \right], \\ &= -\frac{1}{e} \frac{g_2 g_3 G_3 - G_2 G_3 g_3 - g_1 G_3 G_4 - g_1 G_3 g_4 + g_1 G_3 G_4 + G_1 g_3 G_4}{f} (\mu_L - \mu_R), \end{split}$$

simplifying, we obtain the expression for the spin current in the system:

$$I_s = -\frac{1}{e} \frac{G_3 g_3 (g_2 - G_2) - g_1 g_4 G_3 + g_3 G_1 G_4}{f} (\mu_L - \mu_R). \tag{C.19}$$

Note that if we now impose $g_2 = g_3$ and $G_2 = -G_3$ due to Onsager reciprocity, we get

$$I_s = -\frac{1}{e} \frac{g_3^2 G_3 + g_3 G_3^2 - g_1 g_4 G_3 + G_1 G_4 g_3}{f} (\mu_L - \mu_R), \tag{C.20}$$

where the third term on the numerator changes with the magnetization of the ferromagnet due to its linear dependence on P_F , and the fourth term changes with chirality handedness due to its dependence on P_t , thus I_s changes with either time-reversal or spatial inversion, expected because of it being the spin current.